

# Drift Wave versus Interchange Turbulence in Tokamak Geometry: Linear versus Nonlinear Mode Structure

Bruce D. Scott

Max-Planck-Institut für Plasmaphysik

EURATOM Association

D-85748 Garching, Germany

*Feb 2001*

The competition between drift wave and interchange physics in general E-cross-B drift turbulence is studied with computations in three dimensional tokamak flux tube geometry. For a given set of background scales, the parameter space can be covered by the plasma beta and drift wave collisionality. At large enough plasma beta the turbulence breaks out into ideal ballooning modes and saturates only by depleting the free energy in the background pressure gradient. At high collisionality it finds a more gradual transition to resistive ballooning. At moderate beta and collisionality it retains drift wave character, qualitatively identical to simple two dimensional slab models. The underlying cause is the nonlinear vorticity advection through which the self sustained drift wave turbulence supersedes the linear instabilities, scattering them apart before they can grow, imposing its own physical character on the dynamics. This vorticity advection catalyses the gradient drive, while saturation occurs solely through turbulent mixing of pressure disturbances. This situation persists in the whole of tokamak edge parameter space. Both simplified isothermal models and complete warm ion models are treated.

PACS numbers:

52.55.Fa—Tokamaks

52.35.Ra—Plasma turbulence,

52.65—Plasma simulation.

## I. Introduction — More Than One Eigenmode in Turbulence

Edge turbulence in tokamak flux tube geometry has been treated by models working from a drift wave [1,2] or resistive ballooning [3,4,5] paradigm. Beyond computing edge transport, the main purpose of these computations is to understand the underlying physical character of the turbulence: drive and saturation mechanisms and free energy transfer channels.

The pure situation of drift wave turbulence is slab geometry in a sheared magnetic field, and all of its basic processes can be found in the simplified two dimensional models in which it was first studied [6,7,8,9,10,11]. The idealised state is one of adiabatic electrons, towards which the electron dynamics parallel to the magnetic field  $\mathbf{B}$  tends:

$$n_e e \mathbf{B} \cdot \nabla \phi \rightarrow \mathbf{B} \cdot \nabla p_e \quad (1)$$

(where equality means the electrons are adiabatic, and where  $\phi$  is the electrostatic potential and  $n_e$  and  $p_e$  are the electron density and pressure, and  $e$  is the electronic charge). This is the adiabatic response, and if it carries all the way to adiabatic electrons there can be no free energy release, because the average transport is zero if there is no phase shift in the direction of the electron drift given by  $-\mathbf{B} \times \nabla p_e$ . The pressure force  $\mathbf{B} \cdot \nabla p_e$  in the Ohm's law conserves energy against the compression of parallel currents along field lines,  $\nabla \cdot (J_{\parallel} \mathbf{B} / B)$ , which provides the back reaction in the electron pressure. Together, these two terms constitute the adiabatic coupling mechanism, which allows the free energy liberated from the background gradient to enter the parallel current. The more familiar Alfvénic coupling with  $\mathbf{B} \cdot \nabla \phi$  then allows the free energy to enter the ExB flow eddies. This is the free energy pathway between the background gradient and the turbulence which gives rise to drift waves, and collectively the adiabatic and Alfvénic couplings constitute the drift wave coupling mechanism  $\tilde{p}_e \leftrightarrow \tilde{J}_{\parallel} \leftrightarrow \tilde{\phi}$  among the respective disturbances. It is important to note in this context that the parallel gradient cannot vanish for finite sized disturbances on closed magnetic flux surfaces (the flux tube geometry is globally consistent [12]), so this adiabatic response is always excited by electron pressure disturbances.

The pure situation of resistive ballooning mode turbulence or ideal ballooning instabilities is an MHD (magnetohydrodynamics) model [13]. In this case, the adiabatic coupling mechanism is specifically neglected so that dissipative Alfvénic activity merely damps  $e\tilde{\phi}/T_e$  towards zero instead of towards  $\tilde{p}_e/p_e$  (here,  $T_e$  is the electron temperature in energy units, and we assume  $p_e = n_e T_e$ ). The only way that free energy can be transferred to ExB motion from the background pressure gradient in an MHD model is

through the magnetic curvature and gradient, which give rise to a finite compressibility of the diamagnetic current and hence the well known interchange effect. In toroidal geometry, this leads to the ballooning mode since the interchange effect is destabilising only on the outer part of the torus, where the radius of curvature and gradient-B vectors become parallel to the pressure gradient. The ideal form of this dynamics as an instability in toroidal geometry was discovered in attempts to explain curious observations of magnetic fluctuations localised to the outboard side of the PLT tokamak [14]. These fluctuations were explained as ideal ballooning modes, which were treated conventionally [15] as well as with what became known as the ballooning transformation [16,17,18]. Resistive ballooning [19] was invoked to explain the existence of tokamak edge turbulence at pressure gradient values below the ideal stability limit and at amplitudes seemingly unattainable by other mechanisms [20,21], and has also been the focus of many linear MHD calculations [22]. More recently [23], the ballooning paradigm was extended to situations including the two fluid Ohm's law (*i.e.*, the adiabatic response), leading to the ballooning mode approach to edge turbulence [3,4,5], coinciding with the development of the earliest treatments of flux tube geometry, which were originally constructed with ballooning modes specifically in mind [24,25].

The new phenomenon which arose with the three dimensional flux tube models is the simultaneous presence of these two quite different types of eigenmode in the same dynamical system. Obviously, there is only one electrostatic potential, so it is not germane to treat both processes separately and simply add up the resulting growth rates and hence mixing length transport estimates (which one could do for linear eigenmodes if the wavenumbers and frequencies were significantly different). We have a situation of ExB turbulence in the presence of a background pressure gradient, which is the basic free energy source for both eigenmode types. What differs is the energy transfer channel, that is, parallel dynamics or interchange forcing. The MHD model contains the interchange mechanism but neglects the drift wave mechanism by omitting the adiabatic coupling. The slab drift wave model neglects the interchange mechanism by omitting the gradient-B and magnetic curvature effects. One must obviously retain these interchange effects in a toroidal model, so the principal consideration becomes the adiabatic response: the neglect of that limits the validity of the MHD model to situations in which the disturbances satisfy  $\tilde{p}_e/p_e \ll e\tilde{\phi}/T_e$  (cf. Eq. 1). For purely parallel (shear Alfvén) dynamics this is satisfied if  $k_{\perp}\rho_s \ll 1$  [26], where  $\rho_s$  is the drift scale at which simple linear drift waves principally occur. However, for ExB motion driven by a pressure gradient, the typical dynamical frequencies are comparable to  $\omega_*$ , the diamagnetic frequency, and hence ExB advection of the pressure will render

$\tilde{p}_e/p_e \sim e\tilde{\phi}/T_e$ , which is the situation of drift waves (note that this does *not* mean adiabatic electrons, as the phase remains arbitrary and the equality need not be very close). The MHD paradigm is therefore not useful in addressing this situation; moreover, it is impossible even to discuss drift waves within MHD due to the missing adiabatic coupling mechanism.

The competition between the two types of eigenmode is strongly complicated by nonlinear physics, when one addresses turbulence. For linear drift waves in the presence of interchange forcing, it can be shown that the interchange forcing can be the principal mechanism leading to a finite parallel current divergence and therefore departures from the adiabatic state, hence phase shift, over a wide range of parameters. This phenomenon is what gave rise to the “drift resistive ballooning” paradigm, in which it was originally attempted to order  $\rho_s$  small in the dynamics [23]. Indeed, the scales of motion in that paradigm are derived from the assumption that interchange forcing balances the parallel current divergence. On the other hand, it was already known that while the linear polarisation drift by itself could only cause a weak nonadiabatic response, the nonlinear dynamics greatly transforms the mode structure of the turbulence [7], leading to robust turbulence even in models with no linear instability at all [10]. Early attempts to treat simple interchange forcing within such models showed that under certain circumstances the interchange forcing did not affect the turbulence even if it could cause significant linear instabilities [27], a result which was confirmed by three dimensional studies [1]. If the nonlinear polarisation drift is strong enough to overcome the interchange forcing in the turbulence, it will provide the balance with the parallel current thereby maintaining electron nonadiabaticity, and the principal scale of motion will vary mostly with  $\rho_s$  even though it is larger than  $\rho_s$ . This is even true in two dimensional slab turbulence, where there is also dependence on dimensionless parameters such as the collisionality [10]. In three dimensional electromagnetic computations, a finite plasma beta was found to enhance the nonlinear drift wave as well as the interchange (ideal ballooning) effects [2]. It therefore becomes crucial to resolve  $\rho_s$  in any computation of tokamak edge turbulence, and crucial further to use a formulation of the magnetic geometry which represents both slab and toroidal mode structure equally well. For the question of what type of mode structure obtains is closely related to which of the polarisation or diamagnetic currents provide the balance with the parallel current under the total divergence.

In this Article we treat the competition between drift wave and interchange physics for control of the turbulence in detail. Firstly working within the simplest model treating both eigenmode types (isothermal electrons, cold ions, where the difference to MHD is in

a single pair of terms) we choose parallel and perpendicular scales typical of edge profiles in modern tokamaks and sweep the plasma beta and collisionality parameters, which is the same thing as varying temperature and density at fixed gradient scale length. We compare the details of the mode structure — amplitude ratios, parallel structure, phase shifts, cross coherence, and drive spectrum — to control cases reflecting the pure situation of both eigenmode types. We also directly measure the details of the vorticity dynamics — mean squared divergences of the pieces of the total current and mean squared transfer effects — to find which two mechanisms are in statistical balance. This gives a rather more complete picture than one would have merely with the usual time traces of transport levels and contour plots showing spatial morphology.

We find that the transitions to both ideal and resistive ballooning turbulence are well defined, and that the “working area” of tokamak edge density/temperature parameter space is occupied by drift wave turbulence. By studying situations where an interchange driven linear eigenmode makes the transition to fully developed turbulence, we also show that the reason for the drift wave character is the nonlinear polarisation drift, which replaces the diamagnetic current as the main balance for parallel currents and nonadiabatic electron activity. It is always dangerous to form one’s insight for turbulence from the properties of linear eigenmodes, and this error is essentially what happened to the drift resistive ballooning paradigm. The conclusions of linear theory are not valid for turbulence, because drift wave turbulence is very much more robust than linear drift waves are: in a variant of the well known ExB shear suppression scenario [28], the rms vorticity level of the turbulence is larger than the ideal interchange growth rate in this steep gradient regime, and so the small scale linear instabilities arising from ballooning effects are superseded by the nonlinear drift wave instability which imposes its own physical character on the dynamics. Finally, though the subject deserves its own treatment in a separate paper, we address the question of the saturation mechanism, with the result that the vorticity nonlinearity always drives while the pressure one provides saturation, as in the pure drift wave case.

## II. The DALF3 Model

The most basic model of ExB drift turbulence containing both drift wave and interchange physics is a four field model in tokamak flux tube geometry which we call DALF3, for three dimensional drift Alfvén turbulence [2]. The magnetic geometry is assumed to be a set of nested, toroidal, axisymmetric flux surfaces, on which one can define a globally consistent flux tube [12]; this is a matter of defining Hamada coordinates aligned to

the equilibrium magnetic field  $\mathbf{B}$  for which there is only one nonvanishing contravariant component, which is a flux function, and applying the parallel boundary condition after one connection length  $L_{\parallel}$ , ensuring that all degrees of freedom in the flux tube actually exist on the flux surface for which it is a model. A technique called “shifted metric” then re-adapts the geometry so as to represent slab and toroidal mode structure equally well, by providing for a perpendicular metric which is locally diagonal within each drift plane perpendicular to  $\mathbf{B}$  [29]. Following the local drift scale ordering, the dependence of the metric on all coordinates except the one parallel to  $\mathbf{B}$  is neglected (cf. Ref. [25]).

The dynamics consists of the fluctuating electrostatic potential ( $\tilde{\phi}$ ) and electron pressure ( $\tilde{p}_e$ ) as state variables, those acting as force potentials, and the parallel current ( $\tilde{J}_{\parallel}$ ) and parallel ion velocity ( $\tilde{u}_{\parallel}$ ) as their corresponding flux variables. Their set of equations is formed by the two conservation laws for charge ( $\nabla \cdot \mathbf{J} = 0$ ) and electron thermal energy, and then the parallel component of the equations of motion for the electrons and ions. The parallel magnetic potential ( $\tilde{A}_{\parallel}$ ) is given by  $\tilde{J}_{\parallel}$  through Ampere’s law, and then  $\tilde{\phi}$  and  $\tilde{A}_{\parallel}$  serve as stream functions for the ExB velocity ( $\mathbf{v}_E$ ) and the magnetic field disturbances ( $\tilde{\mathbf{B}}_{\perp}$ ), respectively. Traditional flute mode ordering is assumed, with parallel and perpendicular components satisfying  $L_{\parallel}^{-1} \sim \nabla_{\parallel} \ll L_{\perp}^{-1} \lesssim \nabla_{\perp}$ , where  $L_{\perp}$  is the perpendicular scale of the background. The background is a set of constant parameters except for where  $\mathbf{v}_E \cdot \nabla$  or  $\tilde{\mathbf{B}}_{\perp} \cdot \nabla$  act on the background pressure gradient. The only nonlinearities are  $\mathbf{v}_E \cdot \nabla$  and  $\tilde{\mathbf{B}}_{\perp} \cdot \nabla$ , the latter which is part of  $\nabla_{\parallel}$ . The derivation is standard; one can consult Ref. [2] for an example (this model is derived from that one by setting  $\tilde{T}_e$  to zero). With the neglect of the temperatures the model is not different from the one by Braginskii [30] under the local drift approximation [31], retaining electromagnetic parallel dynamics [32].

A more general model will be briefly invoked in the Section IX to show that the results are not dependent on the neglect of the temperatures, but the usefulness of DALF3 is its closeness to resistive, reduced MHD: the two models differ only in the presence or absence of the adiabatic coupling mechanism and of the (nearly negligible) diamagnetic heat flux in the pressure equation. This allows investigation of the special effects of the adiabatic  $\tilde{p}_e \leftrightarrow \tilde{J}_{\parallel}$  coupling in direct fashion.

The equations are normalised in terms of drift scales  $\rho_s$  and  $c_s/L_{\perp}$ , defined by

$$\rho_s^2 = \frac{c^2 M_i T_e}{e^2 B^2} \quad c_s^2 = \frac{T_e}{M_i} \quad (2)$$

This is the standard gyro-Bohm normalisation, leading to a diffusion level  $D_{GB} = \rho_s^2 c_s / L_{\perp}$  and a flux velocity level  $\Gamma_{GB} = c_s (\rho_s / L_{\perp})^2$ . The dependent variables are scaled in terms

of  $e\tilde{\phi}/T_e$ ,  $\tilde{p}_e/p_e$ ,  $\tilde{J}_\parallel/n_e e c_s$ , and  $\tilde{u}_\parallel/c_s$ , and the auxiliary one in terms of  $\tilde{A}_\parallel/\hat{\beta} B \rho_s$ , where  $\hat{\beta}$  is one of the parameters discussed below. The dependent variables are further scaled with an additional factor of  $\rho_s/L_\perp$ , such that a normalised  $\tilde{\phi} = 1$  refers to an unnormalised  $e\tilde{\phi}/T_e = \rho_s/L_\perp$ . The parallel gradient and divergence are normalised against  $L_\parallel/2\pi$ , while the perpendicular gradient is normalised against  $L_\perp$ . The normalised equations appear as

$$\frac{1}{B^2} \frac{d}{dt} \nabla_\perp^2 \tilde{\phi} = B \nabla_\parallel \frac{\tilde{J}_\parallel}{B} - \mathcal{K}(\tilde{p}_e) \quad (3)$$

$$\hat{\beta} \frac{\partial \tilde{A}_\parallel}{\partial t} + \hat{\mu} \frac{d\tilde{J}_\parallel}{dt} = \nabla_\parallel (p_e + \tilde{p}_e - \tilde{\phi}) - C \tilde{J}_\parallel \quad (4)$$

$$\frac{d}{dt} (p_e + \tilde{p}_e) = B \nabla_\parallel \frac{\tilde{J}_\parallel - \tilde{u}_\parallel}{B} - \mathcal{K}(\tilde{p}_e - \tilde{\phi}) \quad (5)$$

$$\hat{e} \frac{d\tilde{u}_\parallel}{dt} = -\nabla_\parallel (p_e + \tilde{p}_e) + \mu_\parallel \nabla_\parallel^2 \tilde{u}_\parallel \quad (6)$$

with the Ampere's law

$$\tilde{J}_\parallel = -\nabla_\perp^2 \tilde{A}_\parallel \quad (7)$$

serving as a constitutive relation (since the eigenvalues of  $-\nabla_\perp^2$  are positive,  $\tilde{J}_\parallel$  and  $\tilde{A}_\parallel$  are in essence proportional and can be used interchangeably as dependent variables). Note that in the DALF3 model  $\tilde{p}_e = \tilde{n}_e$  (we thereby avoid the misconception that drift wave dynamics is driven solely by the density gradient — cf. Ref. [10]).

For the present purpose we use the simplified form of the sheared flux tube geometry, neglecting all finite aspect ratio effects except for the existence of the interchange operator  $\mathcal{K}$ . The factors of the magnetic field strength in Eqs. (3,5) are set to unity. The connection length  $L_\parallel$  becomes  $2\pi q R$ , with  $q$  the standard field line pitch parameter and  $R$  the major radius. We use the shifted metric coordinate system [29], which uses a different  $y$ -coordinate at each location in  $s$ , labelled  $y_k$  for the particular field aligned coordinate system which has a locally orthogonal perpendicular Laplacian operator at  $s = s_k$ . When taking derivatives in  $s$  we then have a shift in the  $y$ -coordinate, since the various  $y_k$  are different. The perpendicular differential operators for the  $k$ -th coordinate system at  $s = s_k$  are

$$\nabla_\perp^2 = \frac{\partial^2}{\partial x^2} + \frac{\partial^2}{\partial y_k^2} \quad \mathcal{K} = \omega_B \left( \sin s \frac{\partial}{\partial x} + \cos s \frac{\partial}{\partial y_k} \right) \quad (8)$$

where  $\omega_B$  is a parameter, and the centered partial  $s$ -derivative at  $s = s_k$  is given by

$$\frac{\partial f}{\partial s}(x, y_k - \alpha_k, s_k) = \frac{f(x, y_{k+1} - \alpha_{k+1}, s_{k+1}) - f(x, y_{k-1} - \alpha_{k-1}, s_{k-1})}{s_{k+1} - s_{k-1}} \quad (9)$$

with shifts given by

$$\alpha_k = \hat{s}s_k x \quad (10)$$

and  $\hat{s}$  parameterising the magnetic shear. We note that in each coordinate system  $\mathbf{B} \cdot \nabla y_k = 0$  for the equilibrium  $\mathbf{B}$ , because  $\mathbf{B} \cdot \nabla x = 0$ . We note as well that the shifts do not affect the partial  $y$ -derivative, which is hereafter written without the subscript  $k$ . Similar centered differences are defined at the mid-node positions  $s_{k+1/2}$ , which shift  $y_k$  and  $y_{k+1}$  onto  $y_{k+1/2}$ , as required by the second order upwind numerical scheme (cf. Ref. [33], which adapts the second order MUSCL scheme [34,35] to this problem). Accordingly, the entire set of geometric quantities (metric, magnetic field strength and unit vector, interchange operator) are defined at both nodes and mid-nodes  $k$  and  $k + 1/2$ . It is important to note that the shifting does not merely reverse the field aligning, as with each  $s_k$  a global constant, we still have  $B^y = 0$  since each  $\alpha_k$  is strictly a function only of  $x$ .

The advective and parallel derivatives are given by

$$\frac{d}{dt} = \frac{\partial}{\partial t} + \mathbf{v}_E \cdot \nabla \quad \nabla_{\parallel} = \mathbf{b} \cdot \nabla \quad (11)$$

where  $\mathbf{v}_E$  and  $\mathbf{b}$  have contravariant components given by

$$v_E^x = -\frac{\partial \tilde{\phi}}{\partial y} \quad v_E^y = \frac{\partial \tilde{\phi}}{\partial x} \quad b^x = \hat{\beta} \frac{\partial \tilde{A}_{\parallel}}{\partial y} \quad b^y = -\hat{\beta} \frac{\partial \tilde{A}_{\parallel}}{\partial x} \quad b^s = 1 \quad (12)$$

The appearance of the background  $p_e$  under derivatives represents the gradient drive terms, through

$$p_e = -\omega_p x \quad (13)$$

where  $\omega_p$  is a parameter (note choosing  $\omega_p = 1$  is equivalent to choosing  $L_{\perp} = L_p$ ).

The dependent variables are defined on a domain

$$-\frac{\pi}{AK} < x < \frac{\pi}{AK} \quad -\frac{\pi}{K} < y < \frac{\pi}{K} \quad -\pi < s < \pi \quad (14)$$

where  $K$  and  $A$  are parameters. The boundary conditions are Dirichlet for  $x$  (dependent variables vanish at the boundaries), periodic for  $y$ , and in  $s$  they satisfy

$$f(x, y_{k+N}, s_{k+N}) = f(x, y_k, s_k) \quad (15)$$

where  $N$  is the number of nodes, noting that the two points are on differing coordinate systems, as in the parallel derivatives. The profiles are maintained by boundary source



terms, damping the  $k_y = 0$  component of  $\tilde{p}_e$  by a Gaussian of amplitude 0.1 and a  $1/e$  width of 0.1 times the domain width, centered at each boundary.

The physical parameters are

$$\hat{\beta} = \frac{4\pi p_e}{B^2} \left(\frac{qR}{L_\perp}\right)^2 \quad \hat{\mu} = \frac{m_e}{M_i} \left(\frac{qR}{L_\perp}\right)^2 \quad C = 0.51 \frac{L_\perp}{c_s \tau_{\nu e}} \frac{m_e}{M_i} \left(\frac{qR}{L_\perp}\right)^2 \quad (16)$$

for the dissipative kinetic shear Alfvén dynamics, and

$$\omega_p = \frac{L_\perp}{L_p} \quad \omega_B = \frac{2L_\perp}{R} \quad \hat{\epsilon} = \left(\frac{qR}{L_\perp}\right)^2 \quad (17)$$

for the gradient drive, interchange forcing, and the sound waves, with  $\mu_\parallel$  an arbitrary parallel diffusion coefficient. Here,  $\tau_{\nu e}$  is the standard Braginskii collision time for the electrons [30]. Nominal parameters corresponding to a typical tokamak plasma edge are

$$\hat{\beta} = 1 \quad \hat{\mu} = 5 \quad C = 7.65 \quad \omega_B = 0.05 \quad \hat{\epsilon} = 18350 \quad \hat{s} = 1 \quad (18)$$

with  $\omega_p = 1$ , roughly reflecting physical parameters:

$$\begin{aligned} n_e &= 3 \times 10^{13} \text{ cm}^{-3} & T_e &= 70 \text{ eV} & B &= 2.5 \text{ T} \\ R &= 165 \text{ cm} & L_\perp &= 4.25 \text{ cm} & q &= 3.5 \end{aligned} \quad (19)$$

The grid for all cases consists of  $64 \times 256 \times 16$  equidistant nodes in  $\{x, y, s\}$ , with a domain size of  $20\pi \times 80\pi \times 2\pi$ , respectively ( $K = 0.025$  and  $A = 4$ ). The time step is 0.05, and the initial state is a random phase distribution for  $\tilde{p}_e$ , with amplitude spectrum  $[1 + (k_\perp^2 / \sqrt{128} K^2)^4]^{-1}$  normalised to an rms amplitude of 3.0, and with  $\tilde{\phi} = \tilde{A}_\parallel = \tilde{u}_\parallel = 0$ .

### III. DALF3 Energetics

The physics of turbulence cannot be assessed from transport scalings or pictorial morphology; quantitative diagnostics of the amplitude, energy, and energetics spectra, as well as several cross-variable statistical measurements relating the transported quantities to the ExB flows that transport them, are needed [1,2,10,11,27,33,38,41]. In the present case, the diagnosis of the energy transfer channels between the equations for  $\tilde{p}_e$  and  $\tilde{\phi}$  are among the more important.

Since the energetics of the DALF3 model will form a central part of the analysis, we review it once more, within the treatment of magnetic coordinates just outlined. To form the energy theorem we multiply Eqs. (3–6) by  $-\tilde{\phi}$ ,  $\tilde{J}_\parallel$ ,  $\tilde{p}_e$ , and  $\tilde{u}_\parallel$ , respectively, and

integrate over the spatial domain, assuming that total divergences vanish. We find the following, in which the integration operation is denoted by the angle brackets,

$$\frac{\partial}{\partial t} \left\langle \frac{1}{2} \frac{1}{B^2} |\nabla_{\perp} \tilde{\phi}|^2 \right\rangle = \langle \tilde{J}_{\parallel} \nabla_{\parallel} \tilde{\phi} \rangle - \langle \tilde{p}_e \mathcal{K} \tilde{\phi} \rangle \quad (20)$$

$$\frac{\partial}{\partial t} \left\langle \frac{1}{2} \tilde{J}_{\parallel} (\hat{\beta} \tilde{A}_{\parallel} + \hat{\mu} \tilde{J}_{\parallel}) \right\rangle = \langle \tilde{J}_{\parallel} \nabla_{\parallel} \tilde{p}_e \rangle - \langle \tilde{J}_{\parallel} \nabla_{\parallel} \tilde{\phi} \rangle - C \langle |\tilde{J}_{\parallel}|^2 \rangle \quad (21)$$

$$\frac{\partial}{\partial t} \left\langle \frac{1}{2} |\tilde{p}_e|^2 \right\rangle = - \langle \tilde{J}_{\parallel} \nabla_{\parallel} \tilde{p}_e \rangle + \langle \tilde{u}_{\parallel} \nabla_{\parallel} \tilde{p}_e \rangle + \langle \tilde{p}_e \mathcal{K} \tilde{\phi} \rangle + \omega_p \left\langle -\tilde{p}_e \frac{\partial \tilde{\phi}}{\partial y} \right\rangle \quad (22)$$

$$\frac{\partial}{\partial t} \left\langle \frac{\hat{\epsilon}}{2} |\tilde{u}_{\parallel}|^2 \right\rangle = - \langle \tilde{u}_{\parallel} \nabla_{\parallel} \tilde{p}_e \rangle + \omega_p \hat{\beta} \left\langle \tilde{u}_{\parallel} \frac{\partial \tilde{A}_{\parallel}}{\partial y} \right\rangle - \mu_{\parallel} \langle |\nabla_{\parallel} \tilde{u}_{\parallel}|^2 \rangle \quad (23)$$

The quantities under the partial time derivatives are the ion drift energy, magnetic and electron kinetic energy, thermal free energy, and sound wave energy. Terms appearing in the right sides of two equations with opposite sign represent the transfer channels, while isolated terms reflect the sources and sinks. The only important source is the one in the pressure equation, ExB advection down the gradient. Currents flowing down the gradient cancel out of the energetics, and sound wave motion down the gradient is always negligible. The sinks are resistive friction ( $C$ ), sound wave viscosity ( $\mu_{\parallel}$ ), and the subgrid dissipation resulting from the nonlinearities, especially  $\mathbf{v}_E \cdot \nabla \tilde{p}_e$ , transferring free energy to arbitrarily small scales — out of the spectrum on the high- $k_{\perp}$  side.<sup>1</sup>

There are two ways for free energy to be channelled from the source in the pressure equation into the ExB turbulence: the drift wave mechanism, which couples  $\tilde{p}_e \leftrightarrow \tilde{J}_{\parallel} \leftrightarrow \tilde{\phi}$  through the parallel dynamics ( $\nabla_{\parallel}$ ), and the MHD compression mechanism, which couples  $\tilde{p}_e \leftrightarrow \tilde{\phi}$  directly through the interchange forcing ( $\mathcal{K}$ ). One of our tasks will be to determine which of these is the more prominent. If we remove the  $\mathcal{K}$  terms only the drift wave mechanism is present; if we remove the  $\nabla_{\parallel}(p_e + \tilde{p}_e)$  term in the Ohm's law (Eq. 4) and the  $\nabla_{\parallel} \tilde{J}_{\parallel}$  term in the pressure equation (Eq. 5) only the interchange mechanism is present. These form the two relevant control cases. The linear transfer effects ( $\nabla_{\parallel}$  and  $\mathcal{K}$ ) would proceed unidirectionally for linear or coherent nonlinear systems, but with the  $\mathbf{v}_E \cdot \nabla$  terms providing a quasirandom character the transfer effects should be understood as exchange

---

<sup>1</sup> Conventional treatments treat this through artificial viscosity terms; herein, the subgrid dissipation is an integral part of the numerical scheme; in any case, it is a defining feature of high Reynolds number turbulence, with the total dissipation independent of the size or form of the dissipation operator.

mechanisms — as we will see, their rms levels are often much greater than their mean values.

Half squared amplitude, free energy, and source and sink profiles and spectra can be defined, for example,

$$A_\phi(k_y) = \frac{1}{N_k} \sum_k \frac{1}{N_i} \sum_i \frac{1}{2} \left| \tilde{\phi}(x_i, k_y, s_k) \right|^2 \quad (24)$$

for the half squared amplitude of  $\tilde{\phi}$ , with  $k_y = lK$  for the  $l$ -th Fourier component, and the  $N$ 's giving the number of grid nodes in each dimension. Half squared means simply 1/2 of mean squared; the factor of 1/2 is used because some of the half squared amplitudes (*e.g.*,  $A_p$  for  $\tilde{p}_e$ ) also appear as free energy components. Further details of how these quantities are defined and measured can be found in Refs. [1,10].

#### IV. Drift Wave and Interchange Control Cases

Here we re-examine two dimensional drift wave and interchange turbulence models, in order to provide a control for the analysis below. From the DALF3 model we neglect the  $s$ -direction, and set  $\hat{\beta} = \hat{\mu} = 0$ , substituting the resulting collisional Ohm's law into Eqs. (3,5). We replace  $-C^{-1}\nabla_{\parallel}^2$  with the positive constant parameter  $D$  for the dynamics involving  $\tilde{J}_{\parallel}$ , and neglect sound wave motion. This reverts to the well known Hasegawa-Wakatani model [7] with interchange forcing. We also add a damping term  $\gamma_d \tilde{\phi}$  to allow the interchange case to saturate. The resulting two dimensional control model is

$$\frac{d}{dt} \nabla_{\perp}^2 \tilde{\phi} = D(\tilde{\phi} - \tilde{p}_e) - \omega_B \frac{\partial \tilde{p}_e}{\partial y} - \gamma_d \tilde{\phi} \quad (25)$$

$$\frac{d}{dt} (p_e + \tilde{p}_e) = D(\tilde{\phi} - \tilde{p}_e) - \omega_p \frac{\partial \tilde{\phi}}{\partial y} - \omega_B \frac{\partial}{\partial y} (\tilde{p}_e - \tilde{\phi}) \quad (26)$$

The drift wave version uses  $D = 0.05$  and  $\omega_B = \gamma_d = 0$ , and the interchange version uses  $D = 0$ ,  $\omega_B = 0.05$ , and  $\gamma_d = 0.01$ . For the drift wave model we eliminate the variations of the  $k_y = 0$  components at each time step. Within the single drift plane, we use the same domain size and initial state as in the three dimensional model. We start both models with the given initial state and run to  $t = 1000$ . The time evolution of the half squared amplitudes of  $\tilde{\phi}$  and  $\tilde{p}_e$  are shown for both cases in Fig. 1, demonstrating saturation.

These two models differ fundamentally in the degree of coupling between  $\tilde{p}_e$  and  $\tilde{\phi}$ , and we will now see that this produces an unequivocal distinction in their mode structure. For the saturated stage  $500 < t < 1000$  we show the average cross coherence and the

phase shift probability distribution spectrum between  $\tilde{p}_e$  and  $\tilde{\phi}$  for both models. For the cross coherence we sample  $\tilde{p}_e$  and  $\tilde{\phi}$  at each node in the domain and at 50 equidistant time intervals, normalise each to its standard deviation, and plot the contours of the resulting histogram. For the phase shifts, we sample  $\alpha_{p\phi}(l) = \text{Im} \log(\tilde{p}_{e_l}^* \tilde{\phi}_l)$  for each Fourier component  $k_y = lK$ , at each node in  $x$  and the same 50 equidistant time intervals, and plot the contours of the spectrum of resulting histograms. The signature of the drift wave coupling mechanism is very clear: For the drift wave case the cross coherence is significant and the phase shift distributions are narrow and close to zero (essentially all activity below about  $\alpha_{p\phi} = \pi/4$ ). It is important to note that this affects every mode in the spectrum, not just the dominant drive range of  $k_y \rho_s \sim 0.2$ . For the interchange case we find the opposite situation of nearly no cross coherence and phase shifts close to  $\pi/2$  since every mode is strongly driven.

This is the mode structure information against which we will compare the results of the three dimensional computations. On the other hand, the drive spectra are very similar and it is important to note that these and other information relying principally or solely on the properties of  $\tilde{n}_e$  or  $\tilde{p}_e$  alone cannot distinguish these two eigenmode types.

## V. Direct Comparison of DALF3 to Resistive MHD

We now run computations within the full DALF3 model and compare them to the resistive MHD model at the same parameters. The MHD model is a reduced MHD case, in which under the drift approximation the ExB flow is dynamically incompressible, and so the perpendicular electric field is electrostatic, just as in the drift wave model. The pressure is the total pressure in MHD, but within a cold ion model the total pressure is simply  $p_e$ . The cold ion model without temperature effects is therefore the closest to the corresponding MHD case. The only difference in the physics is the adiabatic coupling mechanism  $\tilde{p}_e \leftrightarrow \tilde{J}_\parallel$ , represented by the terms  $\nabla_\parallel p_e$  in the Ohm's law and  $\nabla_\parallel J_\parallel$  in the equation for  $p_e$ . In the MHD model this coupling is absent, and the diamagnetic flux divergence is neglected in the pressure equation; in all other respects the DALF3 and MHD models are identical (in MHD the distinction between warm or cold ions is lost through the neglect of the diamagnetic flow vorticity and gyroviscosity, and the neglect of the adiabatic coupling mechanism in the electrons). The MHD model appears as

$$\frac{1}{B^2} \frac{d}{dt} \nabla_\perp^2 \tilde{\phi} = B \nabla_\parallel \frac{\tilde{J}_\parallel}{B} - \mathcal{K}(\tilde{p}_e) \quad (27)$$

$$\hat{\beta} \frac{\partial \tilde{A}_\parallel}{\partial t} + \hat{\mu} \frac{d \tilde{J}_\parallel}{dt} = -\nabla_\parallel \tilde{\phi} - C \tilde{J}_\parallel \quad (28)$$

$$\frac{d}{dt}(p_e + \tilde{p}_e) = -B\nabla_{\parallel} \frac{\tilde{u}_{\parallel}}{B} + \mathcal{K}(\tilde{\phi}) \quad (29)$$

$$\hat{e} \frac{d\tilde{u}_{\parallel}}{dt} = -\nabla_{\parallel}(p_e + \tilde{p}_e) + \mu_{\parallel} \nabla_{\parallel}^2 \tilde{u}_{\parallel} \quad (30)$$

with the Ampere's law,

$$\tilde{J}_{\parallel} = -\nabla_{\perp}^2 \tilde{A}_{\parallel} \quad (31)$$

All other considerations are as in Section III. Simple comparison to Eqs. (3–6) shows that the resistive MHD model is an entirely included subset of the DALF3 model.

We run both models with the fixed parameter set shown above, and vary  $C$  from very low to very high values. The cases shown are for  $\nu = \{1, 2, 5, 10, 20, 50, 100, 200\}$ , with  $C = 2.55 \times \nu$ , and  $\mu_{\parallel} = 0$  (allowing the numerical scheme to provide dissipation at the very shortest parallel as well as perpendicular wavelengths). The normalised  $\nu$  is  $L_{\perp}/c_s\tau_{\nu e}$ , and  $C = 0.51\hat{\mu}\nu$ .

The first quantities to show are the practical ones, the transport and the relative amplitudes between  $\tilde{\phi}$  and  $\tilde{p}_e$ , which appear in Fig. 3, with the four main drift wave cases with  $\nu = 1, 2, 5, 10$  checked with doubled resolution in the drift plane. If the MHD model predicted these correctly the DALF3 model would represent an unnecessary level of complication. We find that the transport scaling does in fact disagree, strongly. We also find that the rms amplitude ratios  $\tilde{\phi}/\tilde{p}_e$  disagree. In drift wave dynamics,  $\tilde{p}_e$  and  $\tilde{\phi}$  are held together by the dissipative adiabatic response, but in MHD this Alfvén dynamics dissipates  $\tilde{\phi}$  only. Since MHD neglects the electron pressure in the Ohm's law, it implicitly assumes that  $\tilde{\phi} \gg \tilde{p}_e$  in any situation in which the geometry sets the parallel scale as it does here. But with only  $\tilde{\phi}$  damped by the Alfvén effects, the MHD model actually delivers a result contrary to its validity, that  $\tilde{p}_e > \tilde{\phi}$ . The DALF3 model finds the result of the adiabatic response, namely,  $\tilde{\phi} \sim \tilde{p}_e$ . Both models give a power law for this amplitude ratio at low  $C$ . The position at which these two lines cross defines the regime boundary between the two models. For  $C$  larger than this critical value, both models find  $\tilde{\phi} > \tilde{p}_e$ . It follows that the resistive MHD model is valid only for  $C$  beyond this value. Because the interchange forcing enters through the parameter  $\omega_B$ , we find the boundary for the transition to resistive ballooning turbulence is at

$$\nu_B = C\omega_B = 1.02 \frac{c_s}{R\tau_{\nu e}} \left( \frac{qR}{V_e} \right)^2 \gtrsim 1 \quad (32)$$

The transport curves both reach maxima and would eventually converge for very large  $C$ ; this is due to the fact that both approach two dimensional interchange dynamics moderated

only by sound waves and nonlinear  $\mathbf{v}_E \cdot \nabla \tilde{p}_e$  cascades for values of  $C$  so large that  $\tilde{J}_{\parallel}$  is essentially negligible. Such values are however well out of the parameter range of interest for tokamak edge turbulence.

Beyond the simple scalings, we turn to the mode structure in the transition range given by  $\nu = \{5, 10, 20\}$ . The most important diagnostics are the ones which tell us about the relationship between  $\tilde{\phi}$  and  $\tilde{p}_e$ , since this is where the models are different. In Fig. 4 we examine the cross coherence between  $\tilde{p}_e$  and  $\tilde{\phi}$  for both models. The control cases appear in Section IV for drift wave and interchange turbulence. We find that the MHD model shows uncorrelated behaviour for all three values of  $\nu$ , while the DALF3 model shows moderate correlation even for the largest  $\nu$ . The adiabatic response coupling  $\tilde{\phi}$  to  $\tilde{p}_e$  through  $\tilde{J}_{\parallel}$  is always significant in this parameter range.

Turning to the phase shift distributions for each  $k_y$  component in the spectrum, we find the MHD model predicting the ideally unstable values of  $\alpha_{p\phi} = \pi/2$  for all  $k_y$ , while the DALF3 model shows the transition between 0 and  $\pi/2$  at low  $k_y$  as  $\nu$  is increased. We see why we need these two diagnostics together: the cross coherence reflects the turbulence as a whole, while the phase shift spectrum shows each component. We can see that the transition is in the longer wavelengths, while the cross coherence is influenced also by the smaller scale activity which remains in a drift wave mode structure. In the drift wave regime, however, the entire spectrum functions as a unit, and to the extent the longer wavelengths cannot separate and form the transition to interchange dominated turbulence, the longer wavelengths are controlled by the shorter ones.

For the fundamental reasons for this state of affairs we turn to the energetics. Recall that the only transfer mechanism between  $\tilde{p}_e$  and  $\tilde{\phi}$  in the MHD model is the interchange forcing. For drift wave turbulence in slab geometry this coupling occurs through the adiabatic response, mediated by  $\tilde{J}_{\parallel}$ , and so the free energy liberated from the background gradient can only reach the ExB eddies through the parallel dynamics. In the DALF3 model both coupling mechanisms are available, and so the question arises as to which is most important energetically as well as in the correlations. In Fig. 6, we measure the energy transfer terms affecting the ion drift energy Eq. (20), including the nonlinearity which operates between various wavelengths but within the ion drift energy. The relevant quantities are the rms levels of these transfer channels, since their importance to the turbulence is in their maintenance of each part of the energetics at finite levels, whatever the instantaneous sign. The results may be compared to those for drift wave and for interchange turbulence.

For the drift wave cases the nonlinear polarisation drift ( $\mathbf{v}_E \cdot \nabla \nabla_{\perp}^2 \tilde{\phi}$ ) is largest, followed by the nonadiabaticity ( $\nabla_{\parallel} \tilde{J}_{\parallel}$ ), while the interchange forcing ( $\mathcal{K} \tilde{p}_e$ ) is subdominant. It is especially important to note that the interchange forcing cannot account for the rms level of the nonadiabaticity, while the nonlinear polarisation drift is more than large enough. The nonlinear ( $\mathbf{v}_E \cdot \nabla \nabla_{\perp}^2 \tilde{\phi}$ ) and linear ( $\nabla_{\perp}^2 [\partial \tilde{\phi} / \partial t]$ ) parts of the polarisation drift largely balance each other, with the excess maintaining the nonadiabaticity.

For pure (MHD) interchange turbulence, especially at low collisionality where the resistive dissipation keeps  $\tilde{\phi}$  small, the interchange forcing and parallel current divergence are in rough balance, and when  $\tilde{\phi}$  and hence the polarisation drift is larger, the interchange forcing becomes larger than the nonadiabaticity. In the DALF3 model containing both eigenmode types, the transition from drift wave to interchange transfer dynamics occurs in the  $\nu > 10$  range, at which all three effects are of comparable importance.

We note now as in the end of Section IV the important fact that if we look only at the morphology of one dependent variable,  $\tilde{p}_e$  for example, that we cannot easily see the difference between the two models. We can see this in the spectra and parallel structure, although if we have this data for both  $\tilde{p}_e$  and  $\tilde{\phi}$  the conclusion is obvious. We show the amplitude spectra for the same six cases, in Fig. 7. The spectra of  $\tilde{p}_e$  look quite similar for the three cases  $\nu = \{5, 10, 20\}$  in both models, but the relationship to  $\tilde{\phi}$  is different. In Fig. 8 the drive spectra are shown, and these too are very similar. Most importantly, the scale of motion is not a distinguishing factor between the two models. *This means that experiments that measure the statistics or morphology only of density fluctuations, which are the most accessible in a hot plasma, can do little to ascertain what the dynamics of the turbulence actually is.*

We find a similar state of affairs in the parallel structure. The amplitude envelopes of the state variables are shown in Fig. 9, and the variation of the transport flux with  $s$  is shown in Fig. 10, each for the same six cases (for these parallel structure figures the  $k_y = 0$  mode is stripped so as to concentrate on the part of the disturbances which lead to net transport down the gradient, noting that  $v_E^x = -\partial \tilde{\phi} / \partial y$ ). Here we find that the outboard to inboard asymmetry of the density disturbance activity is also not a distinguishing factor, as the mere presence of interchange forcing, even at the low levels implied by  $\omega_B = 0.05$ , is sufficient to make a difference in the overall dynamics. But this difference is a quantitative difference. The important part of the parallel structure is the much lower degree of asymmetry in  $\tilde{h}_e$  compared to either  $\tilde{\phi}$  or  $\tilde{p}_e$  in the DALF3 model. Although  $\tilde{p}_e$  is strongly ballooned, the quantity which actually liberates free energy is actually  $\tilde{h}_e$ , whose relative lack of ballooning in DALF3 for  $\nu_B \lesssim 1$  reflects the importance of field line

connection and drift wave coupling. The fact that  $\tilde{p}_e$  (or  $\tilde{\phi}$ ) is ballooned is actually not very relevant to the question of what type of turbulence this is.

Taking all these diagnostics together, the qualitative difference of the DALF3 model with  $\nu_B < 1$  to the two dimensional slab drift wave model is negligible. Although the presence of the interchange effects is noticeable, the omission of the adiabatic  $\tilde{p}_e \leftrightarrow \tilde{J}_{\parallel}$  coupling leads to catastrophic changes. The basic mode structure features which are able to tell the difference between drift wave and interchange turbulence decide the contrast unequivocally for drift wave mode structure, and therefore dynamics, for the regime described by  $\nu_B < 1$ .

## VI. The Role of Interchange Forcing in Drift Wave Turbulence

It is instructive to examine the effect of the interchange terms, which do the interchange forcing, on simple linear drift waves with prescribed, constant  $k_{\perp}$  and  $k_{\parallel}$ . This version of the linearised equations takes a single Fourier component by setting  $\nabla_{\perp}^2 \rightarrow -k_{\perp}^2$ , and  $\nabla_{\parallel} \rightarrow ik_{\parallel}$ , and  $\partial/\partial y \rightarrow ik_y$ , and for the interchange forcing  $\mathcal{K} \rightarrow i\omega_B k_y$ . To find the fate of the instabilities, all we need to know is the response of  $\tilde{h}_e$  to  $\tilde{\phi}$  in order to find the dispersion relation, because the resulting phase shift is closely related to the linear growth rate. The vorticity equation and Ohm's law, Eqs. (3) and (4), are all we need. Using the relations  $\omega_* = \omega_p k_y$  and  $\omega_c = \omega_B k_y$ , their linearised form is

$$\omega k_{\perp}^2 \tilde{\phi}_{\mathbf{k}} = k_{\parallel} \tilde{J}_{\parallel \mathbf{k}} - \omega_c \tilde{p}_{e\mathbf{k}} \quad (33)$$

$$\hat{\beta} (\omega - \omega_*) \tilde{A}_{\parallel \mathbf{k}} + (\hat{\mu}\omega + iC) \tilde{J}_{\parallel \mathbf{k}} = -k_{\parallel} (\tilde{p}_{e\mathbf{k}} - \tilde{\phi}_{\mathbf{k}}) \quad (34)$$

Eliminating  $\tilde{J}_{\parallel \mathbf{k}}$ , we find the equation for the response. It is simplest to do this in the collisional regime, where  $C$  is the dominant effect in Eq. (34). We then find

$$\tilde{p}_{e\mathbf{k}} = \frac{k_{\parallel}^2 - iCk_{\perp}^2\omega}{k_{\parallel}^2 + iC\omega_c} \tilde{\phi}_{\mathbf{k}} \quad (35)$$

As with drift waves proper, the consideration of the phase shift is only important when  $k_{\parallel}$  is finite, enough so that  $k_{\parallel}^2$  is the largest term in both numerator and denominator of Eq. (35). If this is so, then the phase shift is small. It then follows that the eigenmode has the same properties as a drift wave, merely with a different excitation mechanism for the phase shift. But the role of the interchange forcing in this case is simply to excite a phase shift and thereby cause the turbulence to be driven by the background gradient. This is the same role the polarisation drift has for drift waves, and the same role its nonlinear version, the vorticity nonlinearity, has for drift wave turbulence. Even in this regime dominated



by parallel dynamics, the interchange effects can assume control and change the mode structure if they dominantly cause the phase shift. We note here that the finiteness of  $k_{\parallel}$  for finite  $k_y$  is guaranteed by the combination of magnetic shear and toroidal topology (closed flux surfaces), that is, field line connection [12].

## VII. Linear versus Nonlinear Mode Structure

The reason that the result of this investigation for the turbulence is so different than what one might expect by looking at linear instabilities is that the nonadiabatic character of drift waves, especially, is greatly changed by their associated nonlinearities. The one with the strongest effect is the nonlinear polarisation drift — equivalently, the self advection of unsteady ExB vortices, or eddies — which is the mechanism through which the turbulence has such strengthened parallel current dynamics, and hence more net nonadiabaticity of the electrons than those linear eigenmodes. This is the reason for and importance of the distinction between drift waves and drift wave turbulence.

We can investigate this directly by starting the dynamics with an initial state in the linear stage with a linear instability strongly driven by the interchange forcing, and then tracking the evolution of the mode structure through the saturation stage, which is the transition from the linear stage towards the turbulence, and then into the fully developed turbulence in which there is no detailed memory of whatever transpires several correlation times before.

The initial state is the same as before, just with an amplitude of  $a_0 = 3 \times 10^{-10}$  instead of the usual 3.0. We take a single case, that given by the nominal parameters in Eq. (18), but with  $\nu = 10$  (hence  $C = 25.5$  and  $\nu_B = 1.25$ ) and  $\mu_{\parallel} = 0$ . The resolution in the  $x$ -direction is increased fourfold to diminish the effects of linear grid modes (the same domain size as before is used in all three dimensions, but the node count is now  $256 \times 256 \times 16$ ; grid modes result from the failure to resolve the rational surface density in  $x$  for the largest  $k_y$  component on the grid). The time traces of the amplitudes, transport, and energetics are shown in Fig. 11. The linear instability develops, and reaches a constant growth rate which is quite large, about 0.15 in the units of  $c_s/L_{\perp}$  (in which the ideal interchange growth rate is about  $\omega_B^{1/2} = 0.22$ ). When the disturbances reach finite amplitude, the growth rate rapidly drops to zero. This is the onset of saturation (the exact moment for this case is  $t = 201$ ). Then, the growth rate begins to fluctuate, rises away from zero for a short while, and then approaches zero again up to some statistical fluctuation on the scale of a correlation time. This is the mode structure adjustment

stage, beginning for this case with the next rise of  $\Gamma_T$  above zero at  $t = 212$  and ending at  $t = 345$  with the next drop of  $\Gamma_T$  back to zero. The transport overshoots before settling, peaking near  $t = 200$ , quickly dropping by half to about  $t = 210$ , and then slowly strengthening throughout the adjustment stage until statistical saturation is reached after about  $t = 400$  for the turbulence and after  $t = 600$  for the larger scale ExB flows. For lower  $C$  the linear instability is confined to rather smaller scales, with more immediately efficient nonlinear decorrelation, and the overshoot is barely noticeable. In either case, the transport and overall growth rate reach statistical saturation only some several  $\Delta t = 100$  after initial saturation, by which time the drive and amplitude spectra have their final form. (Preliminary studies of these effects with only  $32 \times 128$  grid nodes in the drift plane showed much stronger overshoot, with a longer period of statistical fluctuation before saturation — by comparison to the result shown here with full resolution one can conclude such behaviour is a manifestation of too few degrees of freedom in the turbulence.) This is the stage of fully developed turbulence, which we can see has a very distinct separation in time from the prior two stages. Full saturation also occurs only after the zonal flows (the  $k_y = 0$  and  $k_{\parallel} = 0$  component of  $\tilde{\phi}$ ), to which the turbulence is energetically coupled [36,37], reach statistical equilibrium, in this case after about  $t = 600$ .

These time traces show evidence for complete supersession of the linear instability by the drift wave turbulence. The last frame (lower right) of Fig. 11 compares the rms vorticity (mostly at  $0.3 < k_{\perp} \rho_s < 1.0$ ; see below) to the linear growth and nonlinear drive rates. In the conventional mixing picture of turbulence driven by a linear instability, the amplitude grows until the nonlinear rms vorticity  $\Omega_{\text{rms}}$  (where  $\Omega = |\nabla \times \mathbf{v}_E| = \nabla_{\perp}^2 \tilde{\phi}$ ) is comparable to the linear growth rate  $\gamma_L$ . The eddies comprising the turbulence are then said to be driven by the instability and decorrelated nonlinearly by their vorticity, leading to the estimates of linear mixing length models:

$$\gamma_L \sim k_{\perp} \mathbf{v}_{k_{\perp}} \quad D_{\text{mix}} \sim \frac{v_{k_{\perp}}}{k_{\perp}} \sim \frac{\gamma_L}{k_{\perp}^2} \quad (36)$$

where  $D_{\text{mix}}$  is the turbulent diffusivity. In this situation, however, we have found not only that  $\Omega_{\text{rms}}$  is much larger than  $\gamma_L$ , but also that the overall drive rate  $\Gamma_+$  is significantly *lower* for fully saturated turbulence than either the drive or overall growth rates in the linear stage. This means that the turbulence is producing its own vorticity through the process of nonlinear self sustainment [10], and the reason that the linear instability at small scale has so little effect on the turbulence mode structure, as we have seen, is that small scale structures are scattered apart by the vorticity before they can grow. The dynamics therefore does not feel the linear instability in these scales. This is a generalisation of the

ideas of linear mixing length models as well as of the linear ExB shear-suppression scenario [28], simply instead of the instability being suppressed by background ExB vorticity ( $\Omega_E = \partial V_E / \partial x$ ), it is suppressed by turbulent ExB vorticity:

$$\Omega_{\text{rms}} \gg \gamma_L \implies D_{\text{scatter}} \gg \frac{\gamma_L}{k_{\perp}^2} \quad (37)$$

where  $D_{\text{scatter}}$  is the scattering diffusivity of the turbulence (nonlinear dissipation effect goes mostly through  $\mathbf{v}_E \cdot \nabla \tilde{p}_e$ ). This is the ultimate reason for the mode structure changes from the linear to the turbulent stages, which we now document.

Fig. 12 shows the spatial morphology in the linear, saturation, and fully developed turbulent stages (only 1/4 of the  $y$ -domain is shown). Up until initial saturation, the properties of radial ( $\nabla x$ ) interchange flows are pronounced, with the spatial morphology looking very much like that of buoyancy driven flow plumes (cf.  $t = 191$ ). Initial saturation occurs when the nonlinearity is strong enough to radially displace the density structures and to break up the plumes ( $t \gtrsim 200$ ). The turbulence begins as both these structures and the ExB flows isotropise as a result of both main ( $\mathbf{v}_E \cdot \nabla$  on the state variables) nonlinearities ( $215 \lesssim t \lesssim 230$ ). It then becomes established as the structures and eddies (coupled by the adiabatic response) expand in scale until the various linear and nonlinear transfer processes are in balance ( $400 \sim t \sim 600$ ). The isotropisation process is the same as that observed in the earliest collisional drift wave turbulence computations [7]. On top of the turbulence, the zonal flows develop as eddies serendipitously line up in the  $y$ -direction and then reinforce themselves by tilting the eddies into an energy-losing relationship vis-a-vis the flow [38]; these are visible as vertical stripes in the pattern of  $\phi(x, y)$ . These striking visual changes provide motivation for the statement that the properties of linear instabilities have no *a priori* relevance to the turbulence. But to really find out whether the linear stage is relevant, we have to examine the mode structure in both stages.

The diagnostics we have been using for the turbulence show important differences between the linear, saturation, and fully developed turbulent stages. The dynamical transfer spectra for the ExB vorticity are shown for the transition stage in Fig. 14, noting that the state quickly approaches what we see in Fig. 6. In the linear stage, the nonlinear polarisation drift is obviously negligible and there is a tight balance between interchange forcing and nonadiabaticity (which also shows that the linear polarisation drift, which involves the partial time derivative, is subdominant). As in the interchange turbulence cases, the linear stage of the DALF3 model shows a close balance between interchange forcing and the parallel current divergence. We therefore have an interchange-dominated linear instability. Through the saturation stage, the polarisation drift enters, and in the end state the

polarisation drift has become the dominant cause of the finite  $\nabla_{\parallel} \tilde{J}_{\parallel}$  and hence electron nonadiabaticity  $\tilde{h}_e = \tilde{p}_e - \tilde{\phi}$  and hence the phase shifts necessary for finite free energy access and, ultimately, net transport, both of which are proportional to  $-\oint dy \tilde{p}_e (\partial \tilde{\phi} / \partial y)$ . The parallel structure, displayed in Fig. 15, also shows interesting changes between the linear and turbulent stages. The degree of ballooning, especially in  $\tilde{h}_e$  is markedly reduced in turbulence. Development of the nonlinear mode structure takes longer for this particularly three dimensional signal, following the slowness of the transport of the adiabatic part of the system along field lines, through sound wave dynamics.

Finally, the phase shift distributions are examined in the stages of linear growth, nonlinear structural adjustment, and fully developed turbulence in Fig. 16. For this choice of parameters the linear instability is very strong ( $\gamma_L \approx 0.15$ ), a significant fraction of the nominal ideal interchange growth rate ( $\gamma_I = \omega_B^{1/2} = 0.22$ ). Its dominant range is about  $0.2 < k_y \rho_s < 1.0$ . When this range becomes nonlinear, the first consequence for the phases is that the large phase shifts in the range  $k_y \rho_s > 0.3$  are eliminated, replaced by a wide distribution which also includes negative values. At late times the long wavelength component finds its structure — the frame on the right of Fig. 16 shows the same character as the corresponding case in Fig. 5. Indeed, the saturated state is independent of the previous history beyond a few correlation times; here, the correlation time is about 6, and long term, large scale memory persists no longer than about ten of these. With the short correlation time of the turbulence, the initial state with which the turbulence is reached is not relevant to consideration of its mode structure or underlying dynamics. It follows that this applies also to linear instabilities. Whether these are relevant depends on the particular case and can be demonstrated only by diagnostics taken on the fully developed turbulence in its own context.

In the present case, the interchange forcing is relevant to the longer wavelengths  $k_y \rho_s < 0.1$ , not to the range of largest linear growth rate. The reason is that the rms vorticity of the turbulence is strongly scale dependent, able to supersede the linear instability in the first decade longward of the  $\rho_s$  scale, but quickly reduced in robustness at larger scale due to the factors of  $k_{\perp}$  in the vorticity nonlinearity (note the factors of  $k_{\perp}$  in Eq. 37). This is made clear if we plot the dynamical transfer spectra for the ExB vorticity against  $k_{\perp}$  rather than  $k_y$ , as in Fig. 17. The spectra are normalised to the total ExB energy. The linear growth stage ( $50 < t < 150$ ) shows the linear instability peaking at  $k_{\perp} \rho_s \gtrsim 0.3$ . In the transitional stage ( $200 < t < 250$ ) the vorticity nonlinearity imposes its own character in that same spectral range. In the stage of fully developed turbulence, the larger scales find their saturated state, and in this case the interchange effects clearly

control the range  $k_{\perp}\rho_s < 0.1$ . Whether the turbulence is ultimately of the drift wave or interchange type depends on whether this larger scale range can decouple from the nonlinear vorticity dynamics which is mostly at  $0.3 < k_{\perp}\rho_s < 1.0$ . If the linear effects are important *only* in this small scale range, then the linear instabilities are completely superseded by the turbulence and do not play a role in its dynamics.

The linear analysis shows that  $\omega_B$  is often the dominant effect in creating a nonzero phase shift  $\alpha_{p\phi}$  and hence the linear instability, giving it a ballooning physical (not just morphological) character. But as the linear eigenmode reaches finite amplitude and the nonlinearities emerge, the turbulence not only saturates but changes its physical character. The mechanism maintaining the finite level of the parallel current changes from interchange forcing to the polarisation drift. We saw in the vorticity dynamical spectra in Fig. 6, that in the fully developed turbulence the interchange forcing does not assume control until the collisionality reaches what we found as the resistive ballooning threshold. The threshold is at about

$$(\nu_B)_{\text{crit}} = (C\omega_B)_{\text{crit}} = 1 \quad (38)$$

which is the boundary beyond which the interchange effects overcome the adiabatic response. At that threshold the transport does not sharply change, but the mode structure does so. So we can properly think of this transition as an eigenmode regime boundary, and of the turbulence to the low collisionality side of it as drift wave turbulence.

The supersession of the linear instability spectrum found by the preceding analysis is the same as was recently shown in a detailed study of the drift wave nonlinear instability [39]. Not only does this form of self sustained turbulence cause turbulence in a sheared slab geometry when initialised at finite amplitude [10], it can also impose itself in favour of the linear instability mechanisms provided these are active in the same spectral range. The vorticity dynamics is active principally in the spectral range  $0.3 < k_{\perp}\rho_s < 1.0$ . Linear instabilities in this range are only relevant if they are strong enough to overcome the dynamical rate indicated by the rms vorticity of the turbulence — a reasonable rule of thumb would be a diamagnetic level of vorticity given by

$$\Omega_D = v_D/L_p \quad (39)$$

(unity in normalised units), where  $v_D = c_s\rho_s/L_p$  is the diamagnetic velocity. ExB flow shear must be stronger than this to suppress the turbulence [33]. Short wavelength linear instabilities will be relevant only if

$$\gamma_L > \Omega_D \quad (40)$$

*i.e.*, their growth rate overcomes this. Long wavelength linear instabilities are always relevant because they can easily take over the spectrum against what is in this range a relatively weak vorticity nonlinearity. The result is, though resistive ballooning is not important to tokamak edge turbulence, ideal ballooning and other such large scale MHD instabilities are always relevant.

The result that the turbulence changes character from the initial linear eigenmode due to supersession by vorticity scattering ( $\Omega_{\text{rms}} > \gamma_L$  but with little direct dissipation) is also interesting because the resulting nonlinear drive rate  $\Gamma_+$  is quite smaller than the original  $\gamma_L$ , even for this borderline drift wave/interchange case. It shows that contrary to usual practice (cf. Ref. [23]), the judgement as to whether a linear or nonlinear instability has principal relevance should not rest on which one in its own native model produces the larger anomalous transport coefficient (*i.e.*, net turbulent flux). If a simple comparison is to be made, the one between  $\Omega_{\text{rms}}$  and  $\gamma_L$  is more useful. But one should be careful about the  $k_{\perp}$ -dependence of both, and ultimately a comprehensive set of numerical solutions to the nonlinear equations containing both models is required to make an informed judgement. The same is true of the nonlinear saturation mechanism, to which we now turn.

## VIII. Drive and Saturation Mechanisms

The roles of the principal nonlinearities,  $\mathbf{v}_E \cdot \nabla \nabla_{\perp}^2 \tilde{\phi}$  and  $\mathbf{v}_E \cdot \nabla \tilde{p}_e$ , are the same in toroidal geometry as in pure slab drift wave turbulence. We can show this by comparing the DALF3 model to the two dimensional drift wave model in a simple test in which we remove either of the two principal nonlinearities from the model. As a baseline case we take the DALF3 model run to  $t = 1000$ , well into saturation, for the nominal parameters given in Eq. (18), but with  $\nu = 2$  (hence  $C = 5.1$  and  $\nu_B = 0.25$ ) and  $\mu_{\parallel} = 0$ . Then, we go back to  $t = 500$  and restart with either  $\mathbf{v}_E \cdot \nabla \nabla_{\perp}^2 \tilde{\phi}$  removed (“novor”) or all  $\mathbf{v}_E \cdot \nabla$  nonlinearities except  $\mathbf{v}_E \cdot \nabla \nabla_{\perp}^2 \tilde{\phi}$  removed (“voronly”) or  $\mathbf{v}_E \cdot \nabla \tilde{p}_e$  removed, and run again to  $t = 1000$ . The results are shown in Fig. 18.

The vorticity nonlinearity very strongly excites the turbulence; it does not saturate even for Dirichlet boundary conditions, as without  $\mathbf{v}_E \cdot \nabla \tilde{p}_e$  there is no nonlinear mixing of the pressure. The pressure gradient continues to feed free energy into the disturbances, with the vorticity nonlinearity maintaining sufficient  $\nabla_{\parallel} \tilde{J}_{\parallel}$  for the turbulence to access regions of statistical phase space with substantial phase shifts. The pressure nonlinearity on the other hand does not lead to arbitrarily strong turbulence, but saturates the overall amplitude at a somewhat higher level. The linear instability is back at work in the absence

of the nonlinear polarisation drift, balancing  $\nabla_{\parallel} \tilde{J}_{\parallel}$  with  $\mathcal{K}(\tilde{p}_e)$ . This result obtained for each of the five cases for which it was checked ( $\nu = 1, 2, 5$  for the DW cases and  $\nu = 2, 5$  for the BM cases); in no case does the turbulence saturate through the  $\mathbf{v}_E \cdot \nabla \nabla_{\perp}^2 \phi$  nonlinearity.

There are subtle differences to this result in the two dimensional (2D) systems. Though most of the subgrid dissipation in all the models goes through  $\mathbf{v}_E \cdot \nabla \tilde{p}_e$ , it remains true for the 2D Hasegawa-Wakatani model (where  $-C^{-1} \nabla_{\parallel}^2$  is replaced by the constant  $D$ ) that for many parameter combinations both nonlinearities are required in order to achieve saturation. Nevertheless, the strongest growth is obtained when  $\mathbf{v}_E \cdot \nabla \nabla_{\perp}^2 \tilde{\phi}$  is present but  $\mathbf{v}_E \cdot \nabla \tilde{p}_e$  is absent. The main restriction of the 2D Hasegawa-Wakatani model is that  $\nabla_{\parallel}^2$  cannot change its characteristic magnitude in response to changes in amplitude of the turbulence.

The 2D model in which the nonlinear instability was first demonstrated is the the 2D sheared-slab model, a simple generalisation of the Hasegawa-Wakatani model to incorporate magnetic shear: the collisional, electrostatic limit is obtained by taking  $\hat{\beta} = \hat{\mu} = 0$ , neglecting any dependence in the  $s$ -direction, and replacing  $\nabla_{\parallel}$  with  $x(\partial/\partial y)$ , that is, the coordinate system is not field aligned [10]. In that model the details of the dynamics are complicated by the way  $k_{\parallel}$  is tied to  $x$ ; among the nonlinearities, retaining only  $\mathbf{v}_E \cdot \nabla \nabla_{\perp}^2 \tilde{\phi}$  causes the entire  $x$ -domain of the turbulence to be narrowed (as is the case with adiabatic electron turbulence [9]), while retaining only  $\mathbf{v}_E \cdot \nabla \tilde{p}_e$  causes the  $x$ -domain to spread. These results were found by taking the 2D slab restrictions within the present DALF3 code and running with a resolution of  $128 \times 512$  grid nodes in  $x$  and  $y$ , within the same  $xy$ -domain size of  $20 \times 80$  in units of  $\pi \rho_s$ , respectively. The cases run were  $C = 1, 10$ , and  $100$ . The effects on the morphology due to the absence of one of the nonlinearities was the same as in the 3D model:  $\mathbf{v}_E \cdot \nabla \nabla_{\perp}^2 \tilde{\phi}$  produces isotropic, monopolar vortices in  $\tilde{\phi}$  which excite  $\tilde{p}_e$  unevenly but to large amplitude. In this case however,  $\mathbf{v}_E \cdot \nabla \tilde{p}_e$  by itself can produce the nonlinear instability at much the same level as with both nonlinearities, by acting indirectly through the partial time derivatives on both state variables. These details of nonlinear and drive and saturation deserve their own study (to be produced elsewhere); it suffices here to have presented the broad outlines.

In three dimensions the degrees of freedom represented by  $x$  and  $k_{\parallel}$  are independent, and the situation is clearer: the slab model which one obtains by setting  $\omega_B = 0$  produces the same results [33] both quantitatively and qualitatively as in the toroidal case shown in this Section, except for the effect of the toroidal case's linear instability in the absence of  $\mathbf{v}_E \cdot \nabla \nabla_{\perp}^2 \tilde{\phi}$ . Removal of the vorticity nonlinearity leads to linear drive (in the toroidal case) and saturation. Removal of the pressure nonlinearity leads to ever growing turbulence and

no saturation. The result is that in three dimensions the vorticity nonlinearity always drives and the pressure nonlinearity always saturates. One important consequence is that all scenarios which rely on Kelvin-Helmholtz effects on turbulent flows for saturation of tokamak edge turbulence are ruled out.

### IX. The DALFTI Model and Results for Warm Ion Turbulence

Here we briefly confirm that the foregoing does not depend on the fact that we restricted to a model with isothermal electrons and cold ions. That was done to make the physics of the system as transparent as possible. To put the temperature dynamics back in, we refer to the methods of Ref. [2] to treat the parallel dynamics; the heat fluxes are themselves dynamical variables so that the two pairs of additional dependent variables  $\{\tilde{T}_e, \tilde{q}_{e\parallel}\}$  and  $\{\tilde{T}_i, \tilde{q}_{i\parallel}\}$  are treated on the same self consistent footing as  $\{\tilde{n}_e, \tilde{J}_{\parallel}\}$  in the DALF3 model (in which  $\tilde{p}_e = \tilde{n}_e$ ). This treats time dependent Landau damping, extending the model to the weakly collisional regime in which the Braginskii equations lose validity (mainly by overestimating damping of  $\tilde{T}_e$  and especially  $\tilde{T}_i$ , since the turbulence is about two orders of magnitude faster than the ion collision frequency). We now have  $\tilde{p}_e = \tilde{n}_e + \tilde{T}_e$  and  $\tilde{p}_i = \tau_i \tilde{n}_e + \tilde{T}_i$  as normalised pressure disturbances, where  $\tau_i = T_i/T_e$  gives the warmth of the ions. The only remaining subtlety is gyroviscosity. The form of the diamagnetic cancellation used here is

$$n_i M_i \mathbf{u}_* \cdot \nabla \mathbf{u} + \nabla \cdot \mathbf{\Pi}_* = \nabla \chi \quad (41)$$

in physical units, where  $\mathbf{u}_*$  is the ion diamagnetic velocity,  $\mathbf{\Pi}_*$  is the gyroviscosity tensor (the diamagnetic momentum flux), and  $\chi$  is a scalar involving finite gyroradius effects and divergences of both the heat flux and the ion velocity [40]. The sole effect of the gyroviscosity is to cancel  $\mathbf{u}_*$  in the advection. The resulting normalised equations are [41]

$$\frac{1}{B^2} \left[ \frac{d}{dt} \nabla_{\perp}^2 (\tilde{\phi} + \tilde{p}_i) + (\nabla \mathbf{v}_E) : (\nabla \nabla \tilde{p}_i) \right] = B \nabla_{\parallel} \frac{\tilde{J}_{\parallel}}{B} - \mathcal{K}(\tilde{p}_e + \tilde{p}_i) \quad (42)$$

$$\frac{d}{dt} (n_e + \tilde{n}_e) = B \nabla_{\parallel} \frac{\tilde{J}_{\parallel} - \tilde{u}_{\parallel}}{B} - \mathcal{K}(\tilde{p}_e - \tilde{\phi}) \quad (43)$$

$$\frac{3}{2} \frac{d}{dt} (T_e + \tilde{T}_e) = B \nabla_{\parallel} \frac{\tilde{J}_{\parallel} - \tilde{u}_{\parallel} - \tilde{q}_{e\parallel}}{B} - \mathcal{K}(\tilde{p}_e - \tilde{\phi}) - \frac{5}{2} \mathcal{K}(\tilde{T}_e) \quad (44)$$

$$\frac{3}{2} \frac{d}{dt} (T_i + \tilde{T}_i) = B \nabla_{\parallel} \frac{\tau_i (\tilde{J}_{\parallel} - \tilde{u}_{\parallel}) - \tilde{q}_{i\parallel}}{B} - \tau_i \mathcal{K}(\tilde{p}_e - \tilde{\phi}) + \frac{5}{2} \tau_i \mathcal{K}(\tilde{T}_i) \quad (45)$$

$$\hat{\beta} \frac{\partial \tilde{A}_{\parallel}}{\partial t} + \hat{\mu} \frac{d \tilde{J}_{\parallel}}{dt} = \nabla_{\parallel} (p_e + \tilde{p}_e - \tilde{\phi}) - \hat{\mu} \nu_e \left[ \eta \tilde{J}_{\parallel} + \frac{\alpha_e}{\kappa_e} (\tilde{q}_{e\parallel} + \alpha_e \tilde{J}_{\parallel}) \right] \quad (46)$$



$$\hat{\epsilon} \frac{d\tilde{u}_{\parallel}}{dt} = -\nabla_{\parallel}(p_e + p_i + \tilde{p}_e + \tilde{p}_i) + \mu_{\parallel} \nabla_{\parallel}^2 \tilde{u}_{\parallel} \quad (47)$$

$$\hat{\mu} \frac{d\tilde{q}_{e\parallel}}{dt} + a_{Le}(\tilde{q}_{e\parallel}) = -\frac{5}{2} \nabla_{\parallel}(T_e + \tilde{T}_e) - \frac{5/2}{\kappa_e} \hat{\mu} \nu_e (\tilde{q}_{e\parallel} + \alpha_e \tilde{J}_{\parallel}) \quad (48)$$

$$\hat{\epsilon} \frac{d\tilde{q}_{i\parallel}}{dt} + a_{Li}(\tilde{q}_{i\parallel}) = -\frac{5}{2} \tau_i \nabla_{\parallel}(T_i + \tilde{T}_i) - \frac{5/2}{\kappa_i} \hat{\epsilon} \nu_i \tilde{q}_{i\parallel} \quad (49)$$

with current, pressures, and temperature ratio

$$\tilde{J}_{\parallel} = -\nabla_{\perp}^2 \tilde{A}_{\parallel} \quad \tilde{p}_e = \tilde{n}_e + \tilde{T}_e \quad \tilde{p}_i = \tau_i \tilde{n}_e + \tilde{T}_i \quad \tau_i = T_i/T_e \quad (50)$$

and Landau damping operators

$$a_{Le} = \hat{\mu}^{1/2} \left(1 - 0.2 \nabla_{\parallel}^2\right) \quad a_{Li} = (\tau_i \hat{\epsilon})^{1/2} \left(1 - 0.2 \nabla_{\parallel}^2\right) \quad (51)$$

including linear gradient terms through

$$n_e = -\omega_n x \quad T_e = -\omega_t x \quad T_i = -\tau_i \omega_i x \quad p_e = -(\omega_n + \omega_t) x \quad p_i = -\tau_i (\omega_n + \omega_i) x \quad (52)$$

The geometry is the same as described in Section II. This is called the DALFTI model, extending drift Alfvén turbulence to the warm ion regime with Landau electrons and ions.

The extra parameters describing collisional dissipation are the normalised collisional frequencies,

$$\nu_e = \frac{L_p}{c_s \tau_{\nu e}} \quad \nu_i = \frac{L_p}{c_s \tau_{\nu i}} \quad (53)$$

where the  $\tau_{\nu e, i}$  are the standard Braginskii collision times [30], in which terms the drift wave collisionality is  $C = \eta \hat{\mu} \nu$ . The numerical constants are

$$\eta = 0.51 \quad \alpha_e = 0.71 \quad \kappa_e = 3.2 \quad \kappa_i = 3.9 \quad (54)$$

for pure hydrogen, treating resistivity, the thermoelectric effect, and electron and ion thermal conduction, respectively. With these numbers  $C$  has the same meaning as in the DALF3 model. If the  $\nu_{e, i}$  become arbitrarily large we recover the Braginskii equations, as discussed in Ref. [2], but we are not in that regime for typical tokamak edge parameters, especially for ions.

We briefly report the reconsideration of the cases in Section V for the DALFTI model, with the same nominal parameters as in Eqs. (18), for which  $\nu = 3$ , and with  $\omega_n = \omega_t = \omega_i = \tau_i = 1$  placing the model in the drift wave gradient regime (ion temperature gradient turbulence, with larger values of  $\omega_i/\omega_n$ , will be treated elsewhere; cf. also Refs. [33] and

[41]). The warm ion MHD model is formed analogously to DALF3: the combinations  $\tilde{\phi} + \tilde{p}_i$  and  $\phi - \tilde{p}_e$  are all replaced simply by  $\tilde{\phi}$  (including the background gradient pieces where they appear under  $\mathbf{v}_E \cdot \nabla$  and  $\tilde{\mathbf{B}}_{\perp} \cdot \nabla$ ). In Fig. 19 we find the transport scaling and the relative disturbance amplitudes for cases with various  $\nu$ , with the four main drift wave cases with  $\nu = 1, 2, 5, 10$  checked with doubled resolution in the drift plane. These results may be compared to Fig. 3. Two things should be noted: The results are somewhat clouded by the presence of the ion temperature disturbance,  $\tilde{T}_i$ , which always exhibits interchange dynamics due to the fact that the nominal sound wave transit frequency  $c_s/qR$  is typically smaller than the dynamical frequencies in the range of  $0.2c_s/L_{\perp}$ , so while the interchange effects are relatively weak compared to the turbulence they are still much stronger than the parallel ion dynamics. We also have the fact that  $\tilde{T}_i$  plays no role in the parallel electron dynamics, and is the only state variable for which this is true. Secondly,  $\tilde{p}_e$  includes both  $\tilde{n}_e$  and  $\tilde{T}_e$ , so that the ratio  $\tilde{\phi}/\tilde{n}_e$  is also influenced by changes in the relative role of the temperature and density gradients. This follows from the fact that more nonadiabatic electron dynamics in the stronger turbulence for higher collisionality leads to comparatively stronger effect due to  $\nabla T_e$  [2,10]. Nevertheless, although the transition regime is wider than in cases with pure electron dynamics (cold ions), it still occurs for  $\nu_B$  only slightly less than unity.

The transition to resistive ballooning for these warm ion cases is shown in Figs. 20–22. As  $\nu$  is swept through the values 2, 5, and 10, we find the gradual increase in the amplitude of  $\tilde{\phi}$  relative to the other state variables. In the drift wave regime  $\tilde{T}_e$  roughly has the same structure as  $\tilde{h}_e$  in the DALF3 model (compare with Fig. 9); indeed, just as in slab drift wave turbulence these two quantities control the release of free energy from the electron thermal gradient and hence play the same role in the turbulence [10]. The fact that they are less ballooned than the density or ion temperature (or the transport fluxes) is the reason that drift wave mode structure persists in turbulence in toroidal geometry, just as for  $\tilde{h}_e$  in the DALF3 model. The arrival of the pure MHD regime for  $\nu = 10$  is also facilitated by the contribution of  $\tilde{p}_i$  to the total ion flow stream function,  $\tilde{W} = \tilde{\phi} + \tilde{p}_i$ , and hence the vorticity,  $\nabla_{\perp}^2 \tilde{W}$ . This adds to the power of the total nonlinear polarisation drift and removes the linear forcing terms from dominance at lower collisionality than in a pure MHD model for which the ion flow is just the ExB flow (cf. also [1]). Tests have shown that the presence of the nonlinear gyroviscosity has a large effect in the practical drift wave regime  $1 < \nu < 5$ , but we leave the details of this to a subsequent publication (without the gyroviscosity, the vorticity in Eq. 42 is advected by the total flow expressed with  $\tilde{W}$ , and there is no correction; in contrast to the actual situation, both energy and enstrophy are conserved in the case that gyroviscosity is neglected). Due mostly to the

new effects brought in by the finite ion temperature, the onset of the transition to the resistive ballooning regime is moved to about

$$(\nu_B)_{\text{crit}} = 0.5 \quad (55)$$

that is, downward by about a factor of two, generally reflecting the equal and additive effects of the electron and ion pressures.

## X. The Ideal Ballooning Boundary

Up to now we have focussed on the comparison between drift wave and resistive ballooning turbulence, where only the collisionality is varied. The other boundary is better known: the ideal MHD boundary, which gives the onset of dissipation free ballooning modes called ideal modes [15]. Experimentally this is thought to give the beta limit, which is known both globally and locally [42]. In Fig. 23 we show this for both the DALF3 and DALFTI models, setting  $\nu = 1$  to get a sharper transition. The transport is computed as a flux as before, but this time it is given in terms of the traditional transport coefficients in physical units — ambiguity with regard to the trend is minimised by choosing all gradient scale lengths equal to  $L_\perp$  and by avoiding the effect of hidden normalisation, as the diffusivities scale with  $\rho_s^2 c_s / L_\perp$  and hence with  $(\hat{\beta}/C)^{1/2}$  if  $B$  and the scale lengths are all held fixed. We find a clear boundary in both models though it is accentuated by the presence of  $\tilde{T}_i$ . The jump in the transport appears at different values of  $\hat{\beta}$  because the total pressure differs in the models. The standard ideal MHD stability parameter is

$$\alpha_M = -q^2 R \nabla \beta = \hat{\beta} \omega_B [(\omega_n + \omega_t) + \tau_i (\omega_n + \omega_i)] \quad (56)$$

in both physical and normalised units, where the two combinations in parentheses give the normalised  $\nabla p_e$  and  $\nabla p_i$ , respectively, giving a factor of 4 for these parameters for DALFTI and a factor of 1 for DALF3. The transport amplitude is plotted against  $\alpha_M$ , showing that the effective ideal ballooning boundary for the turbulence is given by

$$0.2 < (\alpha_M)_{\text{crit}} < 0.6$$

for  $\hat{s} = 1$ . The regime change starts closer to 0.2 but the mode structure changes are not complete until the longer wavelengths separate from the rest of the dynamics, for  $\alpha_M$  about 0.6.

The mode structure changes in the ideal ballooning transition are shown in Figs. 24–26, for the three cases  $\hat{\beta} = \{0.3, 1.0, 3.0\}$  for the DALFTI model, measured in the same

way as in Section V. The signature of the change in character of the turbulence is very clear in these figures. When the ideal ballooning takes over, it does so in the longest wavelengths as their phase shifts separate from the rest of the spectrum. At the same parameters, the cross coherence between  $\tilde{n}_e$  and  $\tilde{\phi}$  is lost. The signatures of the change in character of the turbulence in this transition is sharper and clearer than in the one for resistive ballooning. All vestige of drift wave character in the cross coherence and parallel structure diagnostics is lost when the ideal ballooning boundary is crossed. The phase shift diagnostic shows that the long wavelength piece splits off and is no longer influenced by the vorticity dynamics coming from the shorter wavelengths, with the result that the entire spectrum no longer acts as a self consistently causal unit. The same behaviour is exhibited by both the DALF3 and DALFTI models.

The ideal ballooning cases saturate only by depleting the pressure profile: With periodic boundary conditions in  $x$  these cases do not saturate at all, instead forming a wide jet in the  $x$ -direction with  $k_x = 0$  and  $k_y L_x \approx \pi$  where  $L_x = 2\pi/AK$  is the  $x$ -domain width. With Dirichlet boundaries the jet becomes a more or less isotropic cell with  $k_x \approx k_y \approx \pi/L_x$ , saturating only as the resulting flux balances the source terms maintaining the profile in the edge damping zones. This means that saturation proceeds only directly on the profile, with the combined action of the nonlinearities unable to suffice. In no case was the vorticity nonlinearity observed to provide saturation through Kelvin-Helmholtz effects. This has been found to be a feature of the “thin atmosphere” situation with aspect ratio  $A \gg 1$ , contrary to other efforts [4] which use  $A = 1$ , artificially constricting the formation of wide down-gradient flows.

## XI. Summary — Turbulence in Context

What these results show is that it is important to consider the turbulence in context when making judgments about its character, especially when in a situation like this there is more than one possible mode structure into which it can arrange itself. Moreover, it is essential to set up computations with equal regard for the properties of both or all the possible eigenmode types, so that the results are not prematurely anticipated. We find that this physical character undergoes strong changes not only in spatial structure but also in energetics as the linear instability makes the transition into turbulence. Since the turbulence has no detailed memory beyond several (rather short) correlation times, the character the dynamics has in the linear stage is not only not relevant, it delivers an incorrect paradigm as to understanding of the basic nature of the turbulence. This serves to underscore the danger of relying on linear instability theory in the formative stages of a

body of work whose aim is to understand turbulence and transport. The linear instability is relevant whenever it can act on the longer wavelengths (low  $k_{\perp}$ ), where the vorticity nonlinearity is weak, but at high  $k_{\perp}\rho_s \sim 1$  (*i.e.*, “high- $n$  ballooning”) they lose relevance because these short wavelength instabilities are superseded by the self sustained drift wave turbulence. Since this turbulence has an rms vorticity greater than the ideal interchange growth rate, it scatters the linear eigenmodes apart before they can grow (in analogous fashion to the way a background ExB vorticity suppresses instabilities).

The important thing to note about these results is that they all speak together; there are no contradictions. In all cases, the mode structure for low collisionality and low beta exhibits clear drift wave character, and the transition to resistive MHD is found to start for  $\nu > 3$ , which for this choice of parameters corresponds to  $\nu_* = 41$ , where  $\nu_* = (qR/\tau_{\nu_e}V_e)\epsilon^{-3/2}$  and in normalised units  $\nu_* = \nu\hat{\mu}^{1/2}\epsilon^{-3/2}$  or about  $13.6\nu_e$  and  $5.3C$  for the nominal scale ratios in Eq. (18), having assumed an inverse aspect ratio of  $\epsilon = 0.3$ . Therefore, having examined the properties of the turbulence in its native context, we can determine where the MHD model begins to be valid, and where we need the drift wave model not only for computation but for fundamental understanding. Where the MHD model loses validity due to the adiabatic response becoming important, it also loses usefulness as a paradigm, because the basic physics of how the disturbances in pressure and ExB flow communicate undergoes fundamental changes. Generally, MHD character is found when the interchange forcing on the pressure overcomes the adiabatic response. For ideal MHD the regime boundary is the ballooning limit at the critical value of  $\alpha_M = q^2R|\nabla\beta|$  for the particular geometry; in the circular tokamak model it is near  $(\alpha_M)_{\text{crit}} = \hat{s}$ . For resistive ballooning the ideal Alfvén response is replaced by its dissipative MHD limit, and the boundary is near  $\nu_B = C\omega_B = 1$ . The factors of order unity will vary with magnetic geometry and some of the complications of the temperatures, but generally for the low beta and moderate collisionality regime in which fusion plasmas are found, one either finds drift wave turbulence if the equilibrium is steady, or ideal ballooning phenomena when there are disruptive events which typically collapse the pressure gradient.

Concerning the situation of linear instabilities vis-a-vis self sustained drift wave turbulence, we find a general indication that short wavelength ( $k_y\rho_s \gtrsim 0.3$ ) linear instabilities are relevant to the turbulence if and only if their linear growth rates are stronger than the general diamagnetic vorticity level:  $\gamma_L > \Omega_D$ . Long wavelength ( $k_y\rho_s \lesssim 0.1$ ) linear instabilities, on the other hand, are always relevant because the vorticity nonlinearity is relatively weak in that spectral range. Borderline cases can only be decided with well resolved computations assisted by detailed diagnosis.

It is important to note that the question of drift wave or ballooning character is one which is decided by the physical processes responsible for free energy generation, transfer, and saturation, not by the general look and feel of the turbulence which would be a very arbitrary issue. The formative literature for both eigenmode types made very clear statements of what these processes should be, and in order to decide which is most relevant one must diagnose those processes directly and within the context of the turbulence itself. It is precisely that which we have done herein.

## References

- [1] B. Scott, *Plasma Phys. Contr. Fusion* 39 (1997) 471.
- [2] B. Scott, *Plasma Phys. Contr. Fusion* 39 (1997) 1635.
- [3] A. Zeiler, D. Biskamp, J. F. Drake, P. N. Guzdar, *Phys. Plasmas* 3 (1996) 2951.
- [4] B. Rogers and J. F. Drake, *Phys. Rev. Lett.* 79 (1997) 229.
- [5] X. Q. Xu, R. H. Cohen, T. D. Rognlien, and J. R. Myra, *Phys. Plasmas* 7 (2000) 1951.
- [6] A. Hasegawa and K. Mima, *Phys. Rev. Lett.* 39 (1977) 205; *Phys. Fluids* 21 (1978) 87.
- [7] M. Wakatani and A. Hasegawa, *Phys. Fluids* 27 (1984) 611.
- [8] R. E. Waltz, *Phys. Fluids* 28 (1985) 577.
- [9] D. Biskamp and M. Walter, *Phys. Lett. A* 109 (1985) 34.
- [10] B. Scott, *Phys. Rev. Lett.* 65 (1990) 3289; *Phys. Fluids B* 4 (1992) 2468.
- [11] B. Scott, H. Biglari, P. W. Terry, and P. H. Diamond, *Phys. Fluids B* 3 (1991) 51.
- [12] B. Scott, *Phys. Plasmas* 5 (1998) 2334.
- [13] H. Strauss, *Phys. Fluids* 19 (1976) 134.
- [14] A. M. M. Todd, M. S. Chance, J. M. Greene, R. C. Grimm, J. L. Johnson, and J. Manickam, *Phys. Rev. Lett.* 38 (1977) 826.
- [15] H. Strauss, *Phys. Fluids* 20 (1977) 1354.

- [16] B. Coppi, *Phys. Rev. Lett.* 39 (1977) 939.
- [17] J. W. Connor, R. J. Hastie, and J. B. Taylor, *Phys. Rev. Lett.* 40 (1978) 396.
- [18] R. L. Dewar and A. H. Glasser, *Phys. Fluids* 26 (1983) 3038.
- [19] H. Strauss, *Phys. Fluids* 24 (1981) 2004.
- [20] B. A. Carreras, L. Garcia, and P. H. Diamond, *Phys. Fluids* 30 (1987) 1388.
- [21] B. A. Carreras and P. H. Diamond, *Phys. Fluids B* 1 (1989) 1011.
- [22] Two prominent ones are: B. A. Carreras, P. H. Diamond, M. Murakami, J. L. Dunlap, J. D. Bell, H. R. Hicks, J. A. Holmes, E. A. Lazarus, V. K. Pare, P. Similon, C. E. Thomas, and R. M. Wieland, *Phys. Rev. Lett.* 50 (1983) 503; T. C. Hender, B. A. Carreras, W. A. Cooper, J. A. Holmes, P. H. Diamond, and P. L. Similon, *Phys. Fluids* 27 (1984) 1439.
- [23] D. R. McCarthy, P. N. Guzdar, J. F. Drake, T. M. Antonsen, Jr., and A. B. Hassam, *Phys. Fluids B* 4 (1992) 1846; P. N. Guzdar, J. F. Drake, *Phys. Fluids B* 5 (1993) 3712.
- [24] S. C. Cowley, R. M. Kulsrud, and R. N. Sudan, *Phys. Fluids B* 3, 2767 (1991).
- [25] M. A. Beer, S. C. Cowley, and G. W. Hammett, *Phys. Plasmas* 2, 2687 (1995).
- [26] A. Hasegawa and L. Chen, *Phys. Fluids* 19 (1976) 1924.
- [27] B. Scott, in *Plasma Physics and Controlled Nuclear Fusion Research 1992* (IAEA, Vienna 1993), Vol. 2, p. 203.
- [28] H. Biglari, P. H. Diamond, and P. W. Terry, *Phys. Fluids B* 2 (1990) 1; Ch. P. Ritz, H. Lin, T. L. Rhodes, and A. J. Wootton, *Phys. Rev. Lett.* 65 (1990) 2543; T. S. Hahm, *Phys. Plasmas* 1 (1994) 2940; T. S. Hahm and K. H. Burrell, *Phys. Plasmas* 2 (1995) 1648.
- [29] B. Scott, *Phys. Plasmas* 8 (2001) 447.
- [30] S. I. Braginskii, *Rev. Plasma Phys.* 1 (1965) 205.
- [31] F. L. Hinton and C. W. Horton, Jr, *Phys. Fluids* 14 (1971) 116.
- [32] B. Scott, A. B. Hassam, and J. F. Drake, *Phys. Fluids* 28 (1985) 275.

- [33] B. Scott, *Phys. Plasmas* 7 (2000) 1845.
- [34] B. Van Leer, *J. Comput. Phys.* 32 (1979) 101.
- [35] P. Colella, *J. Comput. Phys.* 87 (1990) 171.
- [36] T. S. Hahm, M. A. Beer, Z. Lin, G. W. Hammett, W. W. Lee, and W. M. Tang, *Phys. Plasmas* 6 (1999) 922.
- [37] M. A. Malkov, P. H. Diamond, and A. Smolyakov, *Phys. Plasmas* 8 (2001) 1553.
- [38] B. Scott, *Plasma Phys. Contr. Fusion* 34 (1992) 1977.
- [39] B. Scott, *New J. Phys.* 4 (2002) 52.
- [40] A. Smolyakov, *Canadian J. Phys.* 76 (1998) 321.
- [41] B. Scott, *Contrib. Plasma Phys.* 38 (1998) 171.
- [42] W. Suttrop, M. Kaufmann, H. J. de Blank, B. Brüsehaber, K. Lackner, V. Mertens, H. Murmann, J. Neuhauser, F. Ryter, H. Salzmann, J. Schweinzer, J. Stober, H. Zohm and the ASDEX Upgrade Team, *Plasma Phys. Contr. Fusion* 39 (1997) 2051.



## Figures

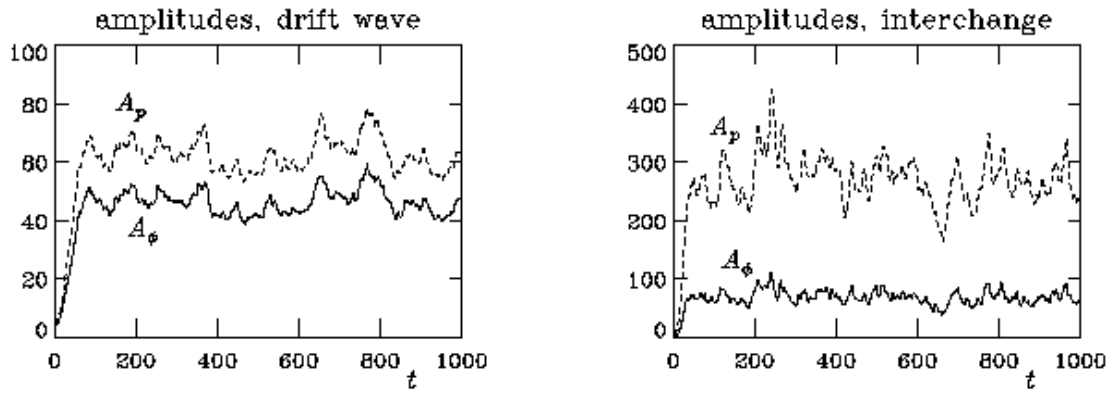


Figure 1. (left) Time traces of the half squared amplitudes of  $\tilde{p}_e$  and  $\tilde{\phi}$ , respectively labelled by  $A_p$  and  $A_\phi$ , in the drift wave model (right) and the interchange model (right), showing saturation. Only in the drift wave model are the time traces for  $A_p$  and  $A_\phi$  similar.

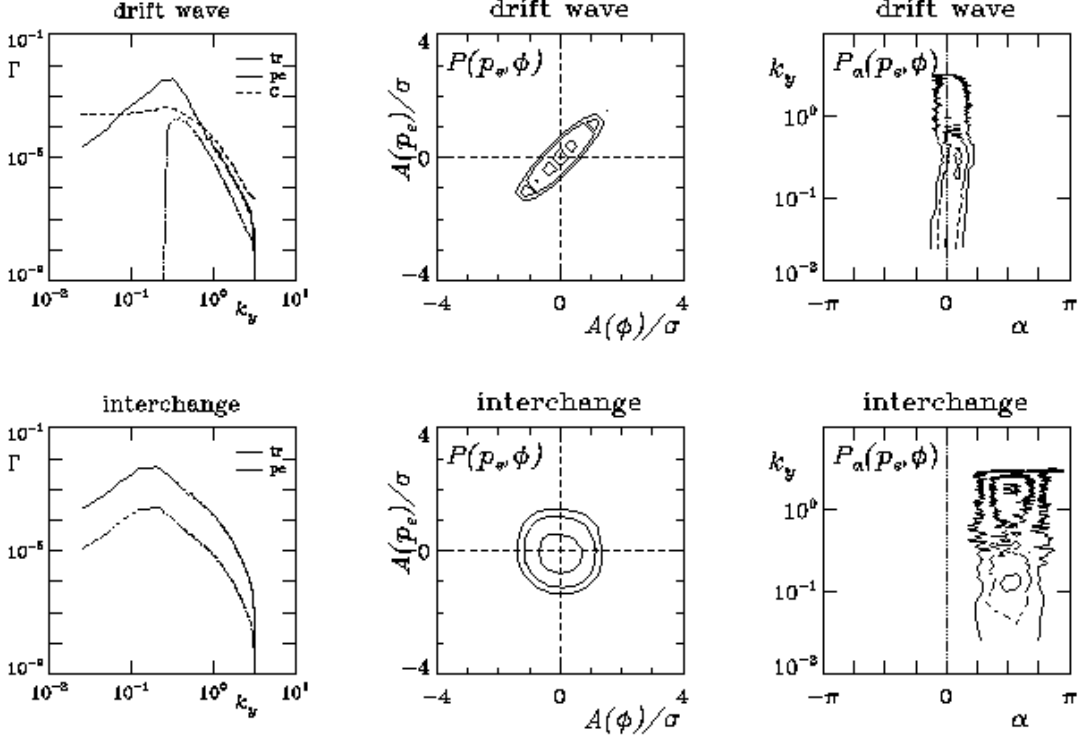


Figure 2. (left to right) Drive and transfer spectra, and cross coherence and phase shifts between  $\tilde{p}_e$  and  $\tilde{\phi}$ , for the drift wave (top row) and interchange (bottom row) models. In the drift wave case the sink spectrum (labelled ‘C’) is relatively flat, and the transfer (‘tr’) is also due to  $\nabla_{\parallel} \tilde{J}_{\parallel}$  and is positive at short wavelength and negative at long wavelength, while in the interchange case it is due to  $\mathcal{K}(\tilde{p}_e)$  which follows the source spectrum (‘pe’). The drift wave case shows strong cross coherence and a narrow phase shift distribution closer to zero than to  $\pi/2$ . The interchange case shows dominance by the longest wavelengths, no cross coherence, and phase shifts near  $\pi/2$  due to the strong driving and weak coupling. The phase shift distributions contours are 0.3, 0.5, and 0.8 times the maximum, and for the cross coherence they are 0.37, 0.5, and 0.8 times the maximum.

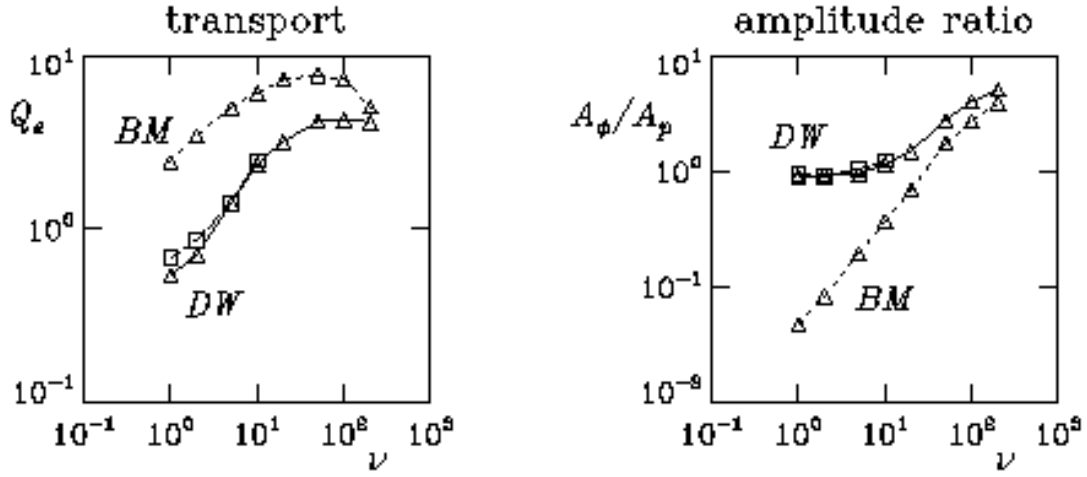


Figure 3. (left) Transport scaling of drift wave and interchange turbulence in toroidal geometry, from the DALF3 and reduced resistive MHD models labelled ‘DW’ and ‘BM’, respectively. The drift wave cases show the clearest scaling with collisionality at low  $C = 2.55\nu$ . At asymptotically large  $C$  the trends will merge, but that limit is not reached. (right) Half squared amplitude ratio (including only  $k_y \neq 0$ ) for the two sets of cases. Due to the adiabatic response,  $\tilde{\phi}$  tracks  $\tilde{p}_e$  for drift wave turbulence, but in the MHD model of the interchange cases  $\tilde{p}_e$  is unaffected by the Alfvén dynamics, and so instead of  $\tilde{\phi}$  being forced towards  $\tilde{p}_e$  it is forced towards zero. The extra points marked with squares for DW ( $\nu = 1, 2, 5, 10$ ) are with double resolution in the drift plane.

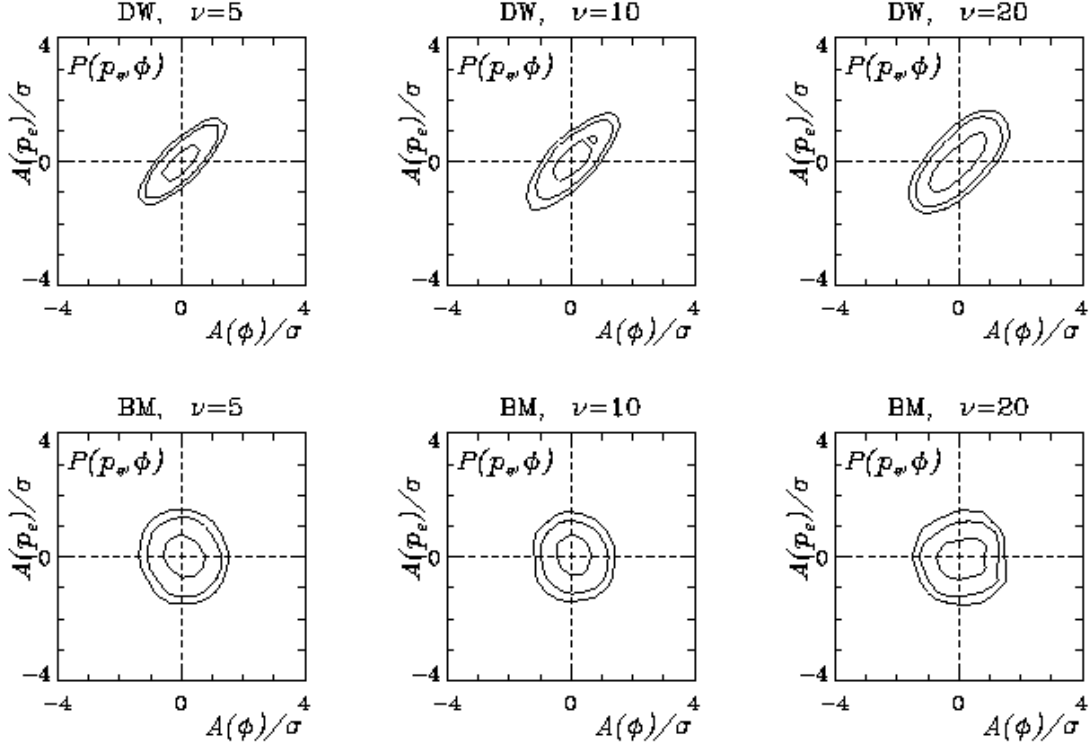


Figure 4. Cross coherence between  $\tilde{p}_e$  and  $\tilde{\phi}$ , for drift wave (top row) and interchange (bottom row) turbulence, for  $\nu = 5, 10$ , and  $20$  (left to right), where  $C = 2.55\nu$  and  $\nu_B = C\omega_B$  as defined in Eq. (32). Compare with the results in Section IV for drift wave and interchange turbulence. The DALF3 model results in drift wave mode structure even for larger  $\nu_B$ , while the MHD model always shows interchange mode structure. Contours are as in Fig. 2.

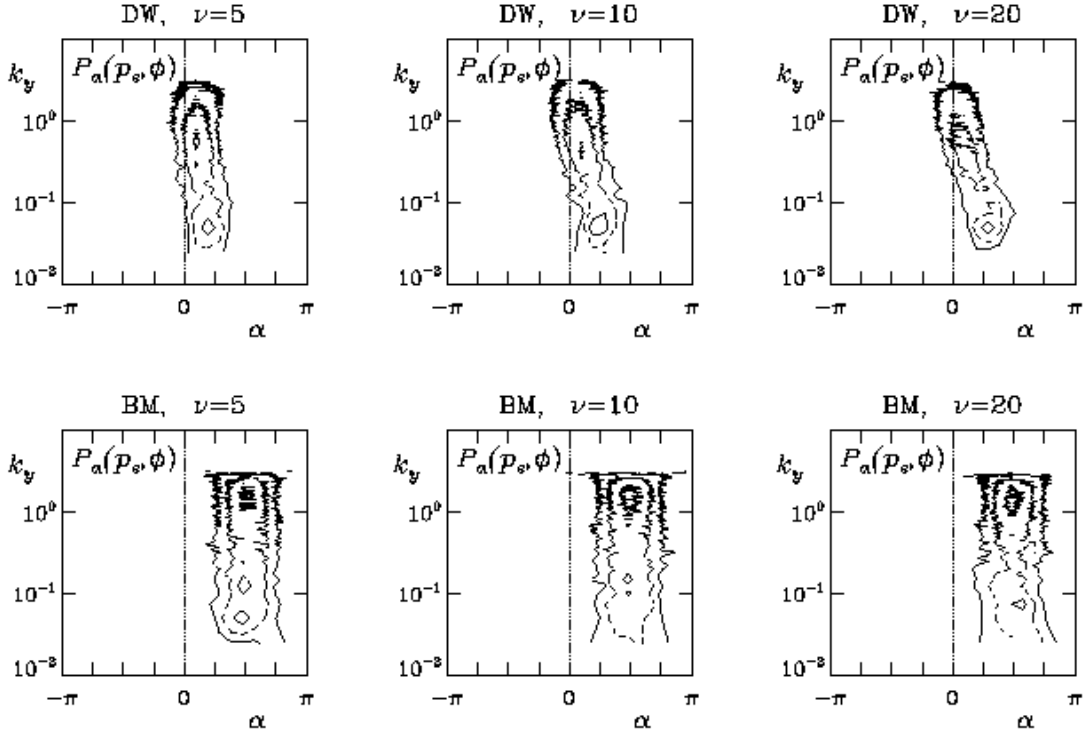


Figure 5. Phase shift distributions of  $\tilde{p}_e$  ahead of  $\tilde{\phi}$  at each  $k_y$ , for drift wave (top row) and interchange (bottom row) turbulence, for  $\nu = 5, 10$ , and  $20$  (left to right), where  $C = 2.55\nu$  and  $\nu_B = C\omega_B$  as defined in Eq. (32). Compare with the results in Section IV for drift wave and interchange turbulence. The DALF3 model results in drift wave mode structure for  $\nu < 10$ , while the MHD model always shows interchange mode structure. The transition to resistive ballooning turbulence in the DALF3 model occurs in the longest wavelengths,  $k_y\rho_s < 0.1$ . Contours are as in Fig. 2.

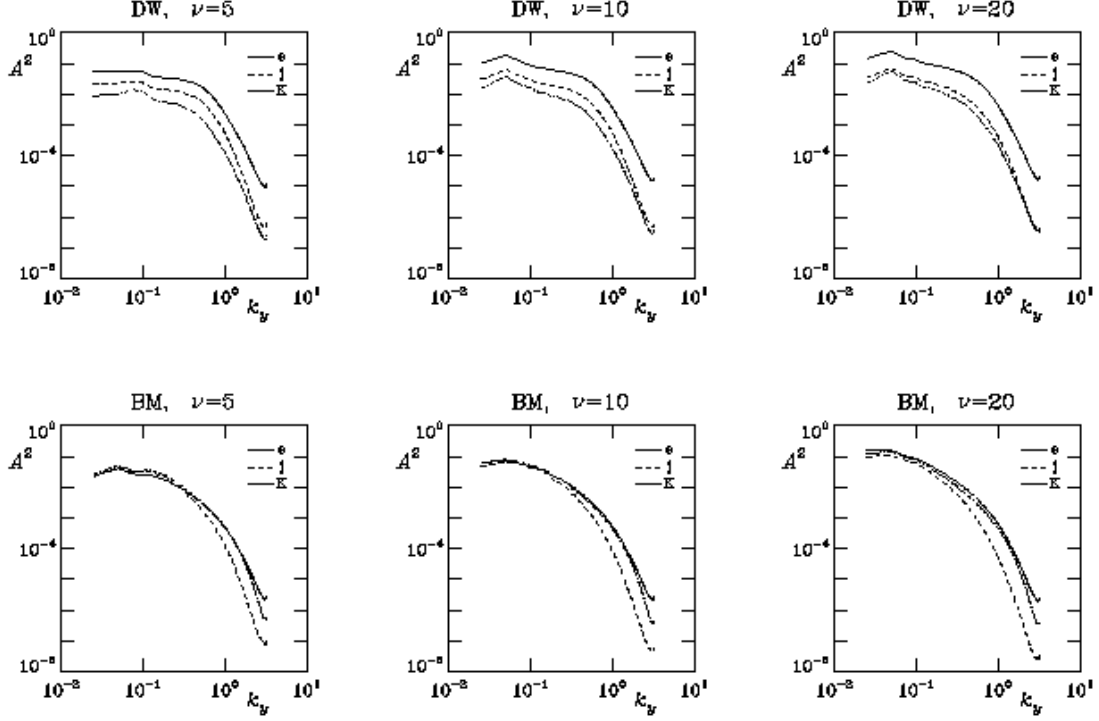


Figure 6. Spectra of the rms transfer dynamical levels for each  $k_y$  in the spectrum, comparing the sizes of  $\tilde{\phi}\nabla_{\parallel}\tilde{J}_{\parallel}$  ('j'),  $\tilde{\phi}\mathcal{K}(\tilde{p}_e)$  ('k'), and  $\tilde{\phi}\mathbf{v}_E \cdot \nabla\nabla_{\perp}^2\tilde{\phi}$  ('e'), for drift wave (top row) and interchange (bottom row) turbulence, for  $\nu = 5, 10, \text{ and } 20$  (left to right), where  $C = 2.55\nu$  and  $\nu_B = C\omega_B$ . In drift wave turbulence the transfer through the current is too large to be accounted for by the curvature, and at all wavelengths the vorticity nonlinearity is balanced only by the linear time derivative. Nonlinear vorticity dynamics is generally much stronger when the adiabatic coupling mechanism  $\tilde{p}_e \leftrightarrow \tilde{J}_{\parallel}$  is present, leading to a self consistent situation in which both mechanisms catalyse each other.

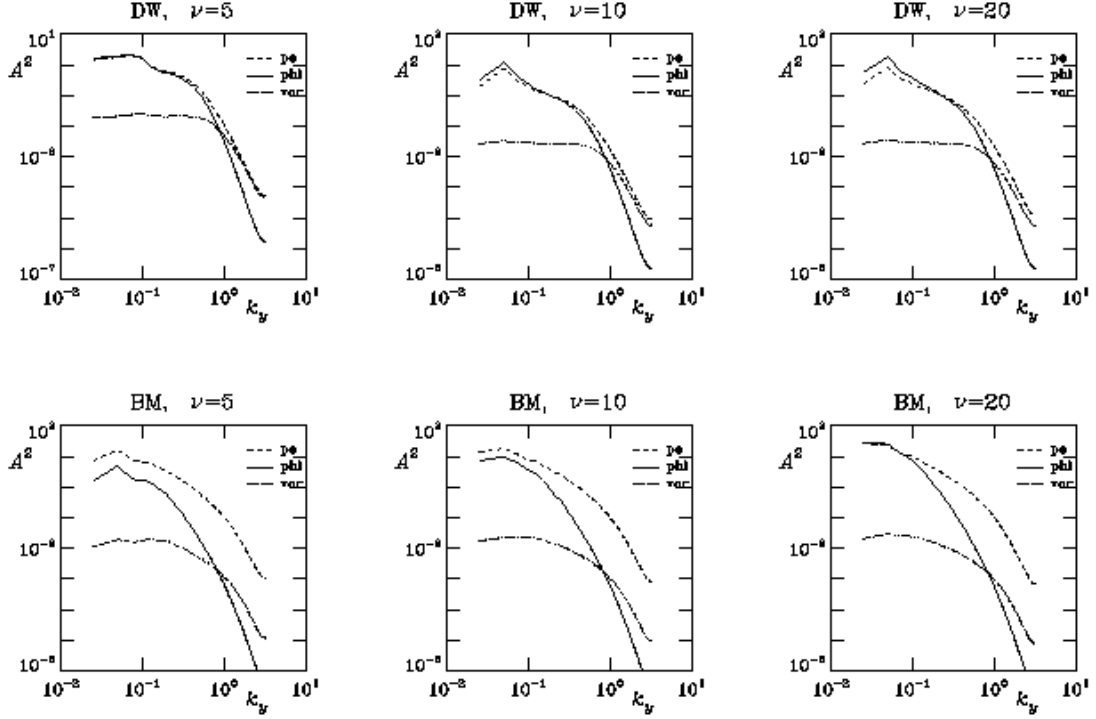


Figure 7. Amplitude spectra of  $\tilde{p}_e$ ,  $\tilde{\phi}$ , and  $\nabla_{\perp}^2 \tilde{\phi}$ , respectively labelled by ‘pe’, ‘phi’, and ‘vor’, for drift wave (top row) and interchange (bottom row) turbulence, for  $\nu = 5, 10$ , and  $20$  (left to right), where  $C = 2.55\nu$  and  $\nu_B = C\omega_B$ . With only the density present one cannot distinguish the mode structure or dynamics, but if  $\tilde{\phi}$  is also present the amplitude ratio, shown in Fig. 3, is decisive, as the spectrum of  $\tilde{\phi}$  follows that of  $\tilde{p}_e$  only for drift wave turbulence. The transition to resistive ballooning turbulence in the DALF3 model ( $\tilde{\phi} \gg \tilde{p}_e$ ) occurs in the longest wavelengths,  $k_y \rho_s < 0.1$ .

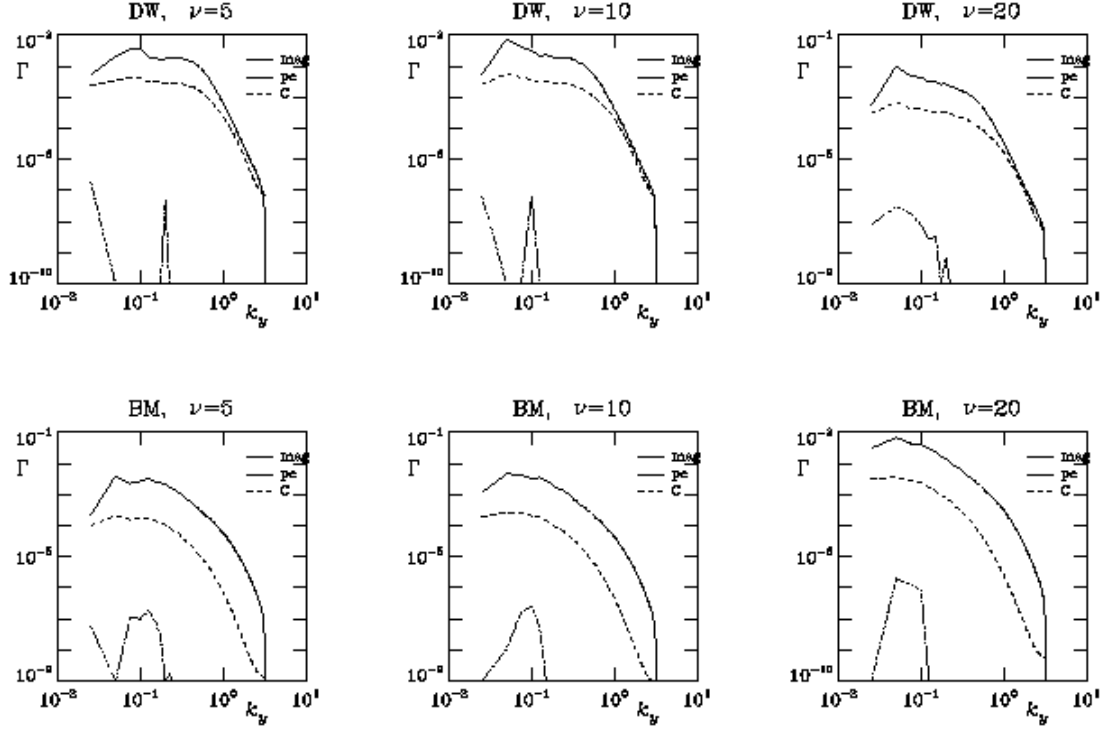


Figure 8. Spectra of the ExB gradient drive (‘pe’), dissipation (‘C’), and the magnetic flutter drive (‘mag’), for drift wave (top row) and interchange (bottom row) turbulence, for  $\nu = 5, 10,$  and  $20$  (left to right), where  $C = 2.55\nu$  and  $\nu_B = C\omega_B$ . For drift wave turbulence the shorter wavelengths contribute more to the energetic drive and hence the ExB transport. Compare the positions of the energy containing range (Fig. 7), the energy producing range (this figure) and the vorticity catalysing range (Fig. 6). These show that for drift wave turbulence the entire spectrum acts as a single unit.



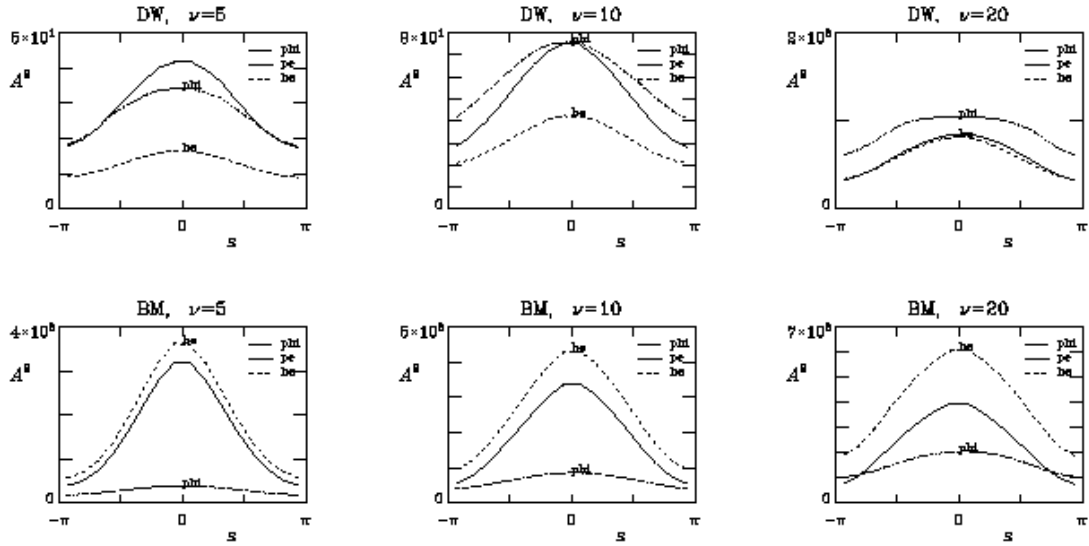


Figure 9. Mean squared amplitude envelopes ( $k_y \neq 0$  only) showing parallel structure of  $\tilde{\phi}$ ,  $\tilde{p}_e$ , and  $\tilde{h}_e = \tilde{p}_e - \tilde{\phi}$ , respectively labelled by ‘phi’, ‘pe’, and ‘he’, for drift wave (top row) and interchange (bottom row) turbulence, for  $\nu = 5, 10$ , and  $20$  (left to right), where  $C = 2.55\nu$  and  $\nu_B = C\omega_B$ . Drift wave mode structure is exemplary for  $\nu < 10$  in the DALF3 model, with  $\tilde{h}_e$  flatter and smaller than either  $\tilde{p}_e$  or  $\tilde{\phi}$ .

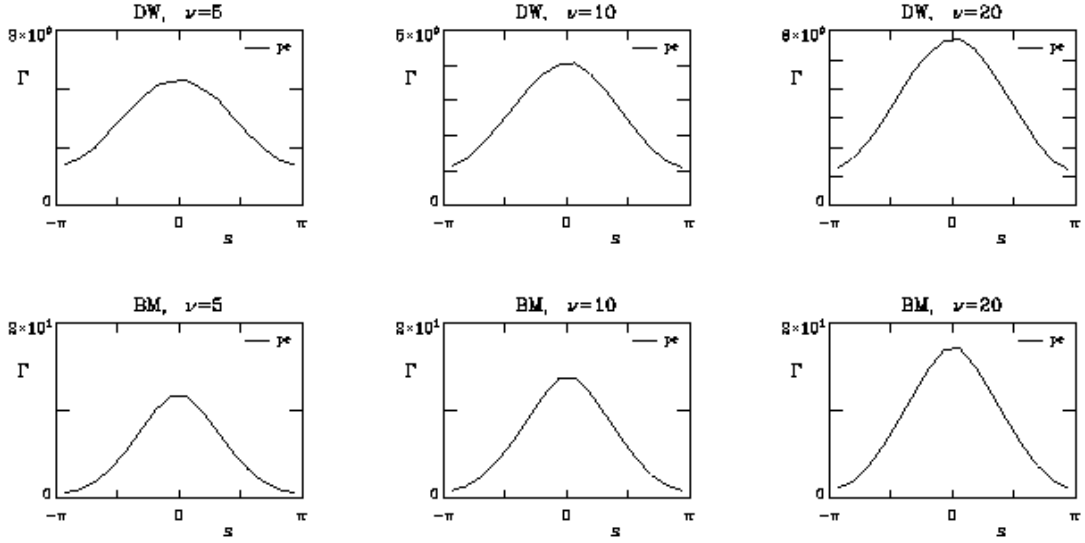


Figure 10. Amplitude envelope of the ExB transport (‘pe’), for drift wave (top row) and interchange (bottom row) turbulence, for  $\nu = 5, 10$ , and  $20$  (left to right), where  $C = 2.55\nu$  and  $\nu_B = C\omega_B$ . The magnetic flutter transport is negligible on this scale. The ballooning in the transport becomes somewhat more pronounced in the transition to interchange character for  $\nu > 10$ , but for all cases the ballooning is much stronger for the MHD model than for DALF3.

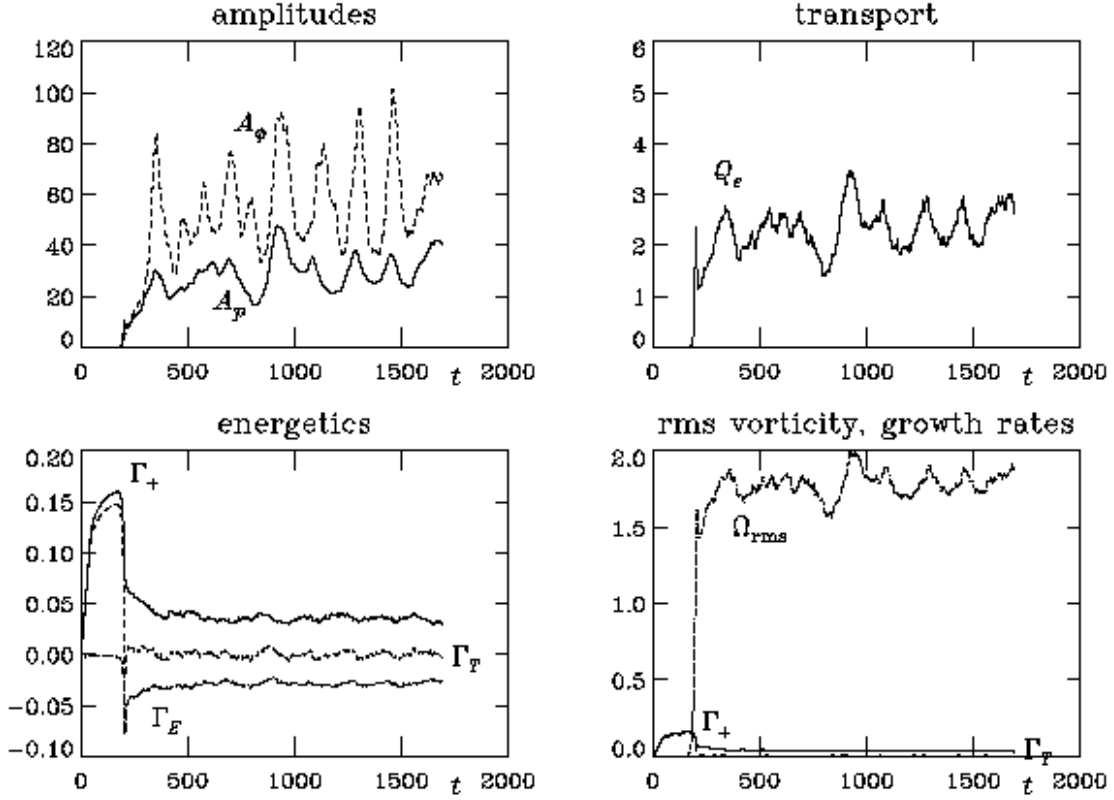


Figure 11. Time evolution of the DALF3 case with  $\nu = 10$  (hence  $C = 25.5$  and  $\nu_B = 1.25$ ) out of a linear initial state at small amplitude, run to  $t = 1582$ . (top left) Half squared amplitudes of  $\tilde{\phi}$  (denoted  $A_\phi$ ) and  $\tilde{p}_e$  ( $A_p$ ). The larger amplitude departures of  $A_\phi$  from  $A_p$  reflect zonal flow activity in the fully developed turbulence. (top right) The transport caused by the turbulence. (bottom left) Growth rate ( $\Gamma_T$ ), gradient drive rate ( $\Gamma_+$ ), and total dissipation rate ( $\Gamma_E$ ). (bottom right) Vorticity (rms) compared to  $\Gamma_+$  and  $\Gamma_T$ . The linear mode leads to overshoot, initial saturation ( $t \approx 200$ ) is reflected in the first drop of  $\Gamma_T$  to zero, and then the nonlinear mode structure takes over shortly thereafter, with full development with robust transport and zonal flow activity established after  $t = 400$ . The turbulence not only saturates but changes character when the rms vorticity overcomes the linear growth rate ( $\gamma_L$ , equal to  $\Gamma_T$  in the linear stage). Nonlinear saturation of the linear instability would obtain if  $\Omega_{rms}$  were comparable to  $\gamma_L$ , but the situation with  $\Omega_{rms} \gg \gamma_L$  indicates complete supersession of the instability by turbulence which has its own dynamics.

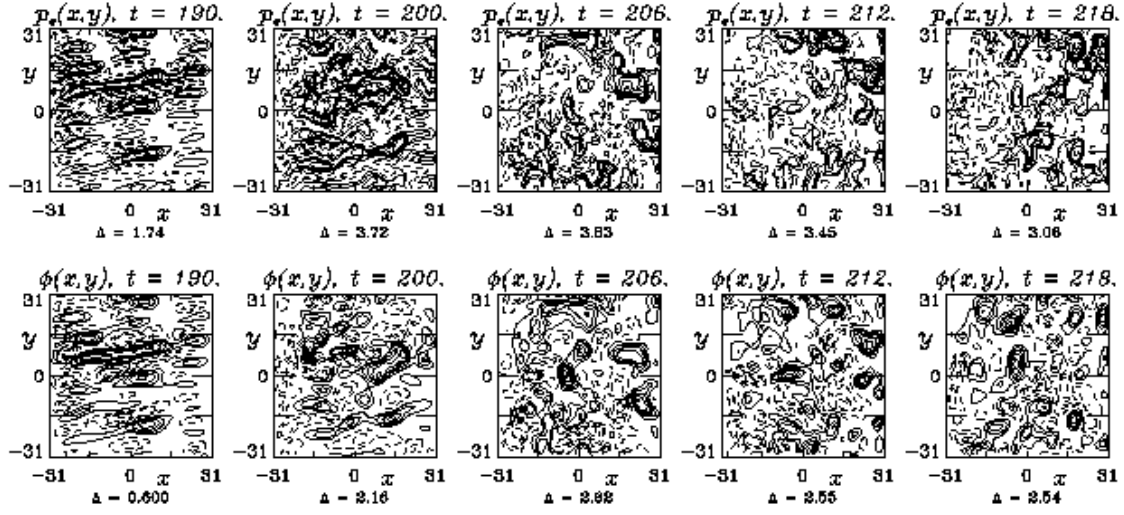


Figure 12. Saturation and initial transition to turbulence, as seen in the spatial morphology of  $\tilde{\phi}$  and  $\tilde{p}_e$  in the linear growth stage to  $t = 190$ , and the initial saturation stage after  $t = 200$ . The transition between linear and nonlinear mode structure is most clear in the disappearance of  $x$ -direction flows reminiscent of buoyant plumes. This represents a transition away from interchange dominated dynamics to a more isotropic turbulence as the vorticity nonlinearity replaces the interchange forcing as the principal mechanism supporting finite parallel currents (nonadiabatic electron dynamics). (Positive/negative values are indicated by solid/dashed lines. Only 1/4 of the computational domain in the  $y$ -direction is shown. The exact moment of saturation is  $t = 201$ , and the growth rate becomes positive again at  $t = 212$ .)

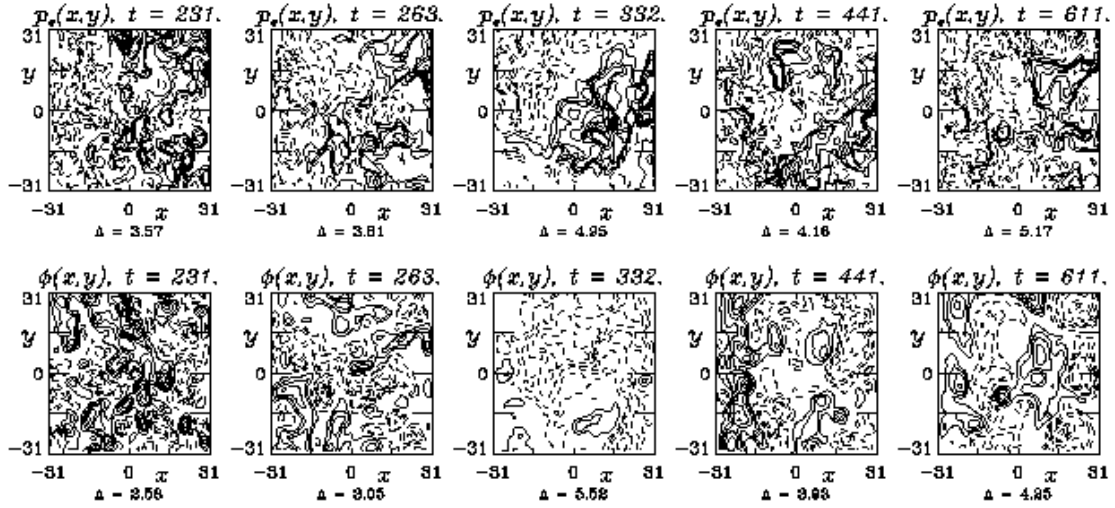


Figure 13. Transition to fully developed turbulence, as seen in the spatial morphology of  $\tilde{\phi}$  and  $\tilde{p}_e$  through the stage of nonlinear structure adjustment, and then in the stage of statistical saturation in which the nonlinear growth rate fluctuates near zero. As the saturated state finds itself, the scale of motion increases, and until  $t = 345$  the nonlinear growth rate is positive. Zonal flows emerge after about  $t = 400$  and reach statistical equilibrium after about  $t = 600$ . The zonal flows are part of the nonlinear mode structure, but by the time they emerge the interchange driven flows of the linear stage are long gone. The correlation time is about 6 in these units. (Positive/negative values are indicated by solid/dashed lines. Only 1/4 of the computational domain in the  $y$ -direction is shown. The exact moment of saturation is  $t = 201$ , and the growth rate becomes positive again at  $t = 212$ , and negative again at  $t = 345$ .)

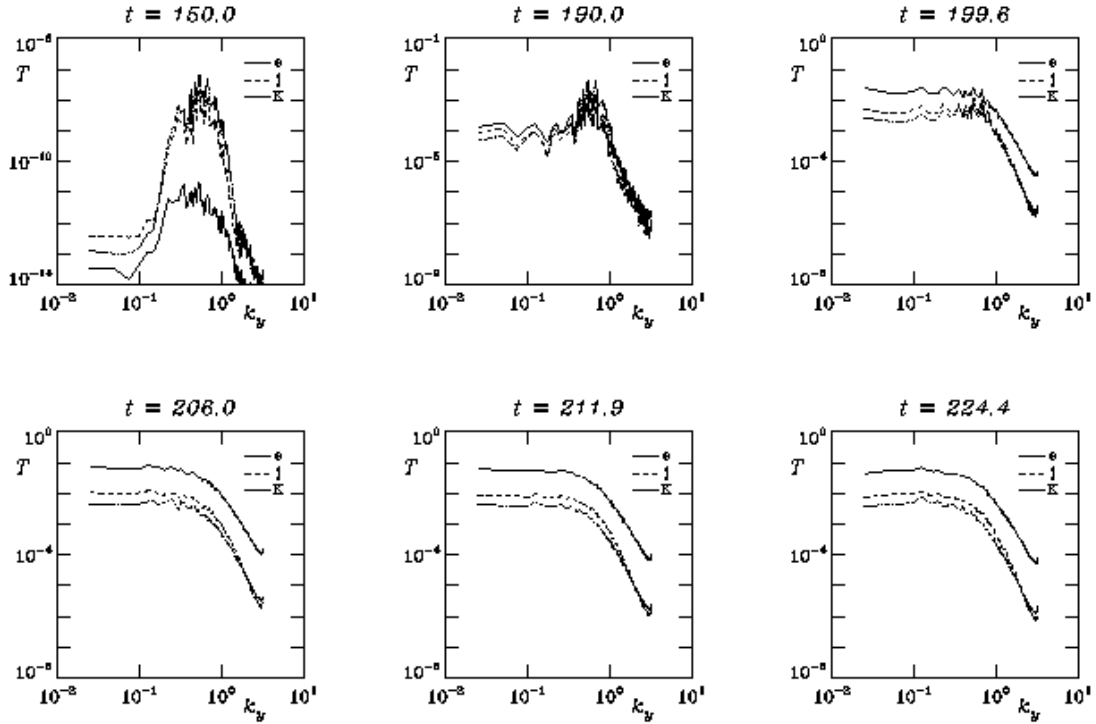


Figure 14. Saturation and transition to turbulence, as seen in the dynamical transfer spectra for the ExB vorticity, for the linear stage to about  $t = 190$ , the saturation stage around  $t = 200$ , and the nonlinear structure adjustment stage after about  $t = 210$ . Compare with Fig. 6. Initially the eigenmode is controlled by interchange forcing, with the linear polarisation drift negligible (cf. Eq. 35). But as the amplitude becomes finite the vorticity nonlinearity, the same one which causes the drift wave nonlinear instability, emerges to become the principal agent supporting nonadiabatic electron dynamics. The transition is extremely rapid, taking place within about one correlation time for the fully developed turbulence. (The exact moment of saturation is  $t = 201$ , and the growth rate becomes positive again at  $t = 212$ , and negative again at  $t = 345$ .)

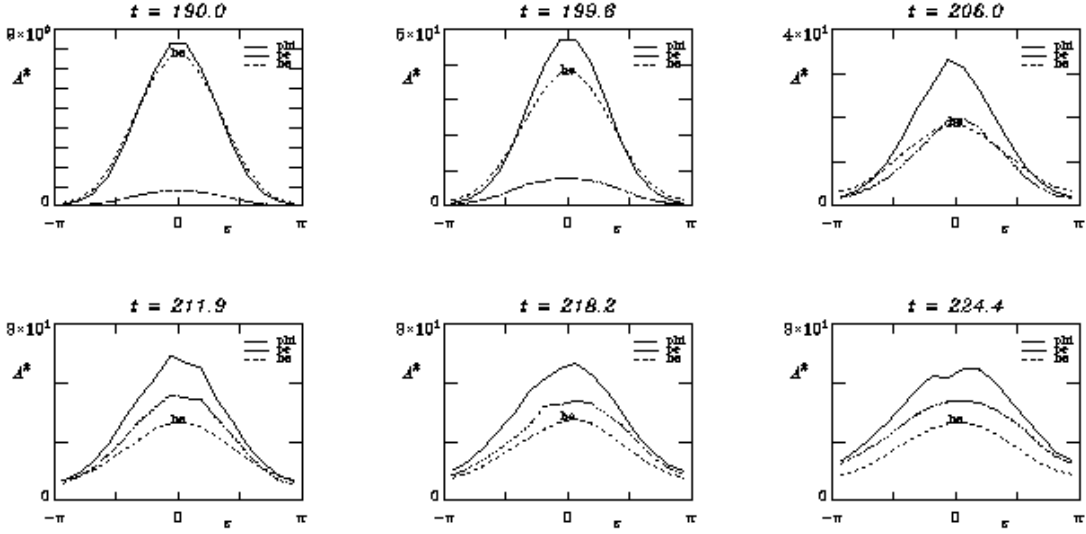


Figure 15. Saturation and transition to turbulence, as seen in the parallel envelope structure ( $k_y \neq 0$  only), in the linear stage to about  $t = 190$ , the saturation stage around  $t = 200$ , and the nonlinear structure adjustment stage after about  $t = 210$ . Compare with Fig. 9. The principal signature of the transition is the emergence of  $\tilde{\phi}$  supported by the vorticity nonlinearity. The interchange flows of the linear stage are eliminated by the turbulent vorticity, and the adiabatic response causes  $\tilde{\phi}$  to track  $\tilde{p}_e$ . The degree of asymmetry is also reduced, especially in  $\tilde{h}_e$ . This transition between linear ( $\tilde{h}_e \sim \tilde{p}_e \gg \tilde{\phi}$ ) and nonlinear ( $\tilde{\phi} \sim \tilde{p}_e \gg \tilde{h}_e$ ) mode structure is almost as rapid as in Fig. 14. (The exact moment of saturation is  $t = 201$ , and the growth rate becomes positive again at  $t = 212$ , and negative again at  $t = 345$ .)

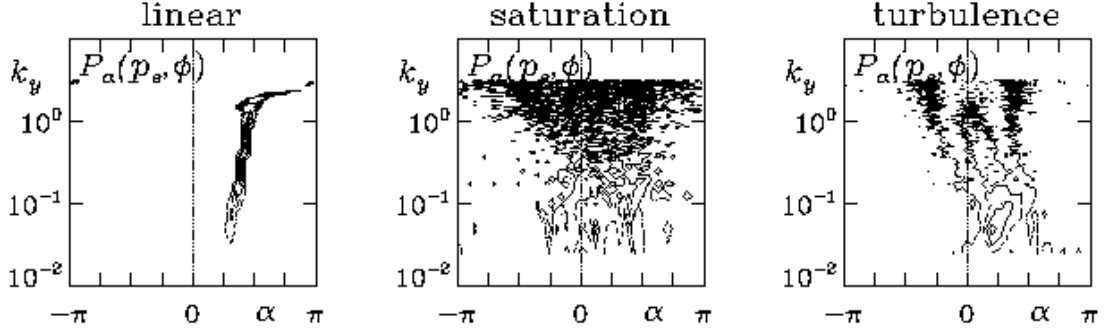


Figure 16. Phase shift distributions of  $\tilde{p}_e$  ahead of  $\tilde{\phi}$  at each  $k_y$ , for the linear stage, averaged over  $50 < t < 150$ , through saturation, averaged over  $200 < t < 244$ , and for the stage of fully developed turbulence, averaged over  $502 < t < 611$ . Compare with Fig. 5. The turbulence emerges to supersede the linear structure with its own, due to the fact that the rms vorticity level of the turbulence is larger than the linear growth rate of the original instability. The linear instabilities in the range  $0.3 < k_y \rho_s < 1.0$  have no role in the turbulence. Only in the fully developed stage does the interchange dynamics for  $k_y \rho_s < 0.1$  emerge to make this case with  $\nu_B = 1.25$  the transitional one between turbulence of the drift wave and interchange type.



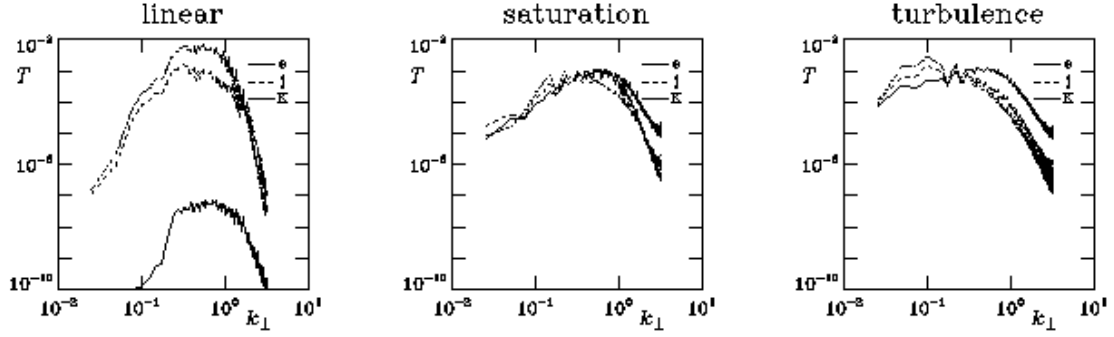


Figure 17. Dynamical transfer spectra for the ExB vorticity, for the linear stage, averaged over  $50 < t < 150$ , through saturation, averaged over  $200 < t < 244$ , and for the stage of fully developed turbulence, averaged over  $502 < t < 611$ , plotted against  $k_{\perp}$  rather than  $k_y$ , showing the scale of motion rather than the wavelength in the drift direction. The linear instability is dominantly in the same range which is later dominated by the turbulence, making the linear interchange dominated mode irrelevant. When interchange effects do enter, as in this transitional case with  $\nu_B = 1.25$ , they do so at larger scale where they more easily overcome the native vorticity of the drift wave turbulence.

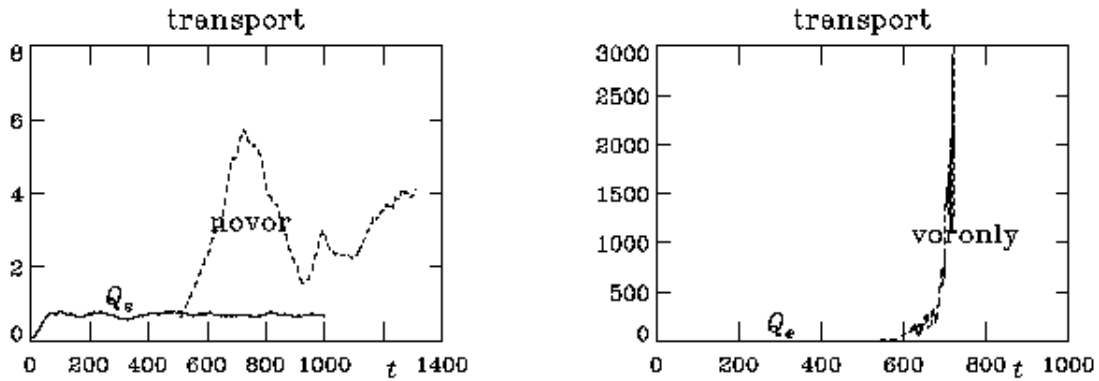


Figure 18. Saturation mechanism in drift wave turbulence in toroidal geometry. The run with  $\nu = 2$  (hence  $C = 5.1$  and  $\nu_B = 0.25$ ) taken to  $t = 1000$  (solid curves) is restarted from  $t = 500$  (dashed curves) with the ExB vorticity nonlinearity either left out ('novor') or with all ExB nonlinearities except the vorticity one left out ('voronly'). Without the vorticity nonlinearity, the linear drive is balanced by mixing via  $\mathbf{v}_E \cdot \nabla \tilde{p}_e$  and saturation occurs. Without the pressure nonlinearity, the vorticity is vigorously scattered via  $\mathbf{v}_E \cdot \nabla \nabla_{\perp}^2 \tilde{\phi}$  with little dissipative effect, and this nonlinear excitation continues indefinitely without saturation.

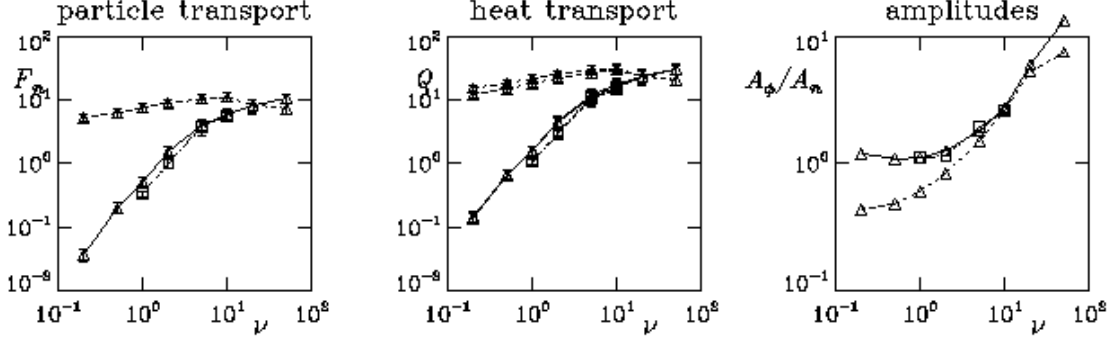


Figure 19. Transport scaling (left two frames) and amplitude ratios (right) of drift wave (solid lines) and resistive MHD (dashed lines) turbulence in toroidal geometry under the DALFTI model. Both ion and electron heat transport are shown as a pair; in each case the ion transport curve is the one lying slightly higher in the pair. The MHD model, which neglects the drift wave coupling terms between  $\tilde{p}_e$  and  $\tilde{J}_\parallel$ , is insensitive to collisionality ( $C = 2.55\nu$ ) because although  $\tilde{\phi}$  is too small,  $\tilde{p}_i$  is too large, compared to the drift wave model. The transition to the MHD regime at a lower  $\nu > 3$  is assisted by the warm ion interchange physics, since  $\tilde{T}_i$  does not feel the adiabatic response. The extra points marked with squares for DW ( $\nu = 1, 2, 5, 10$ ) are with double resolution in the drift plane. Compare with Fig. 3.

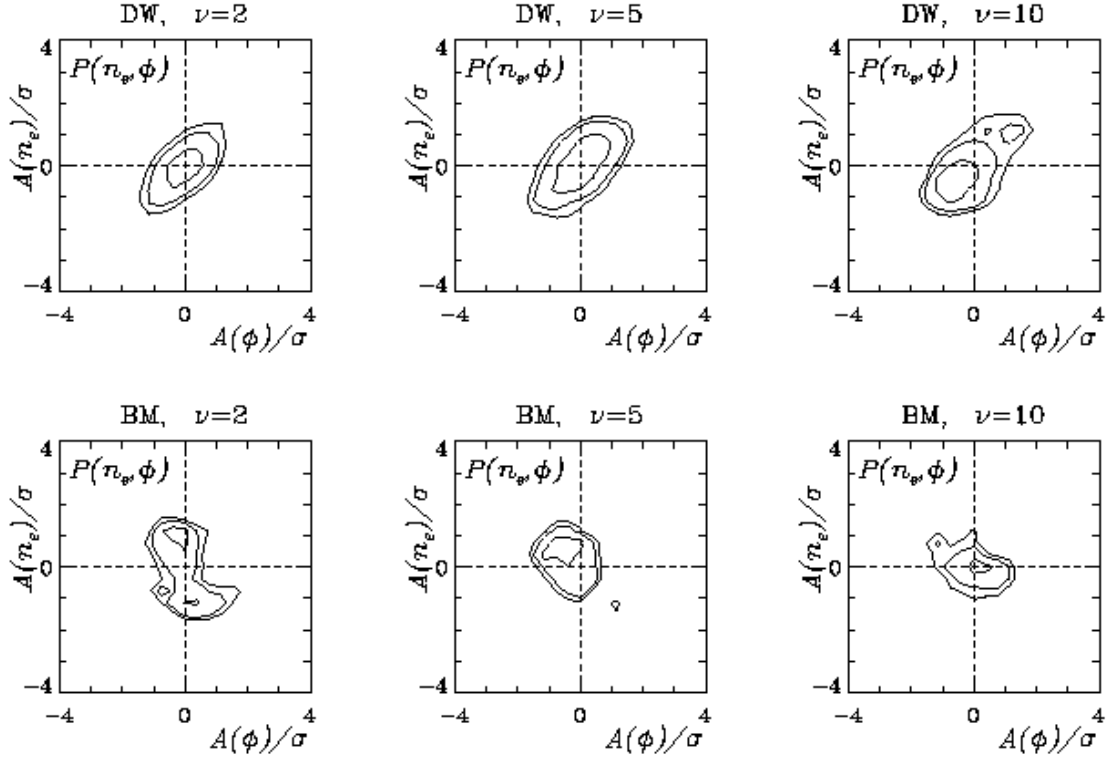


Figure 20. Cross coherence between  $\tilde{n}_e$  and  $\tilde{\phi}$ , for drift wave (top row) and interchange (bottom row) turbulence, for  $\nu = 2, 5$ , and  $10$  (left to right), where  $C = 2.55\nu$  and  $\nu_B = C\omega_B$  as defined in Eq. (32). The turbulence makes the transition from drift wave to resistive ballooning mode structure for  $\nu_B$  of about  $0.5$  (here,  $\nu = 5$ ). Compare to Fig. 4. Interchange turbulence with warm ions is very violent at small scales due to the effects of gyroviscosity, reducing the timestep and shortening the runs.

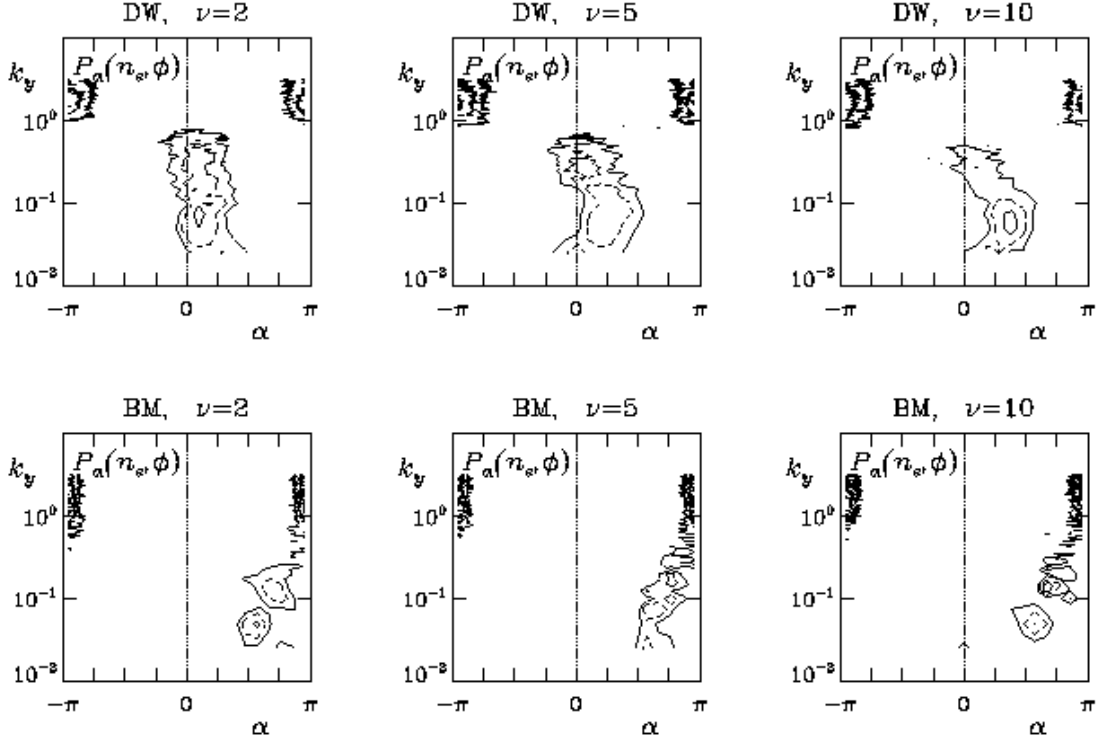


Figure 21. Phase shift distributions of  $\tilde{n}_e$  ahead of  $\tilde{\phi}$  at each  $k_y$ , for drift wave (top row) and interchange (bottom row) turbulence, for  $\nu = 2, 5$ , and  $10$  (left to right), where  $C = 2.55\nu$  and  $\nu_B = C\omega_B$  as defined in Eq. (32). The turbulence makes the transition from drift wave to resistive ballooning mode structure for  $\nu_B$  of about  $0.5$ . Compare to Fig. 5. The tendency of the phase shift to go to  $-\pi$  at small scales is the signature of the nonlinearity in the gyroviscosity which conserves energy but not vorticity for warm ions, producing the effects seen in Fig. 20. As in the DALF3 model, the transition to resistive ballooning turbulence in the DALF3 model occurs in the longest wavelengths,  $k_y\rho_s < 0.1$ .

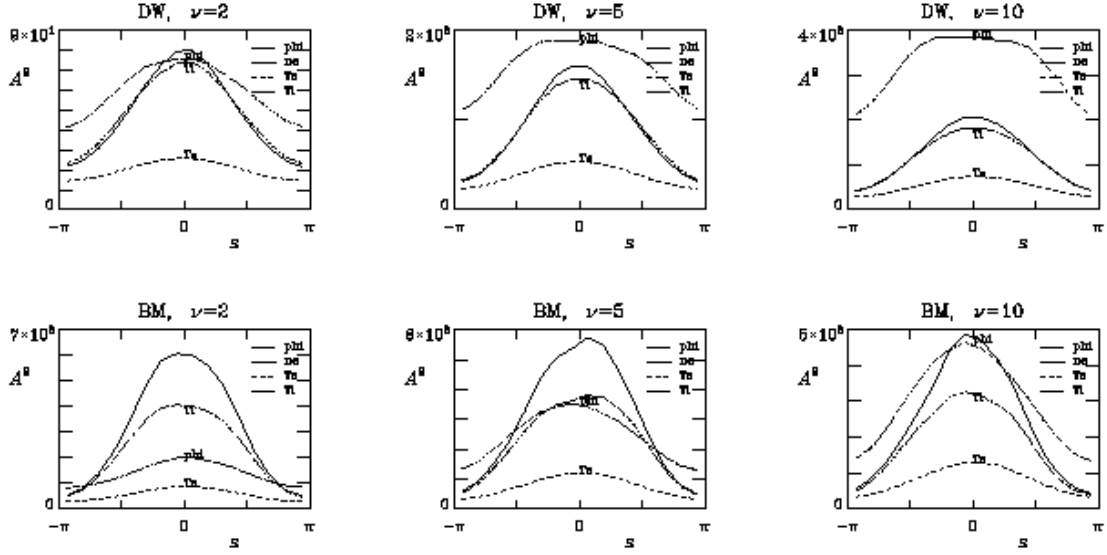


Figure 22. Mean squared amplitude envelopes ( $k_y \neq 0$  only) showing parallel structure of  $\tilde{\phi}$ ,  $\tilde{n}_e$ ,  $\tilde{T}_e$ , and  $\tilde{T}_i$ , respectively labelled by ‘phi’, ‘ne’, ‘Te’, and ‘Ti’, for drift wave (top row) and interchange (bottom row) turbulence, for  $\nu = 2, 5$ , and  $10$  (left to right), where  $C = 2.55\nu$  and  $\nu_B = C\omega_B$  as defined in Eq. (32). The turbulence makes the transition from drift wave to resistive ballooning mode structure for  $\nu_B$  of about  $0.5$ , with additional effects due to the contribution of  $\tilde{p}_i$  to the vorticity, as described in the text. Note  $\tilde{p}_e = \tilde{n}_e + \tilde{T}_e$  and  $\tilde{p}_i = \tau_i \tilde{n}_e + \tilde{T}_i$  in this model.

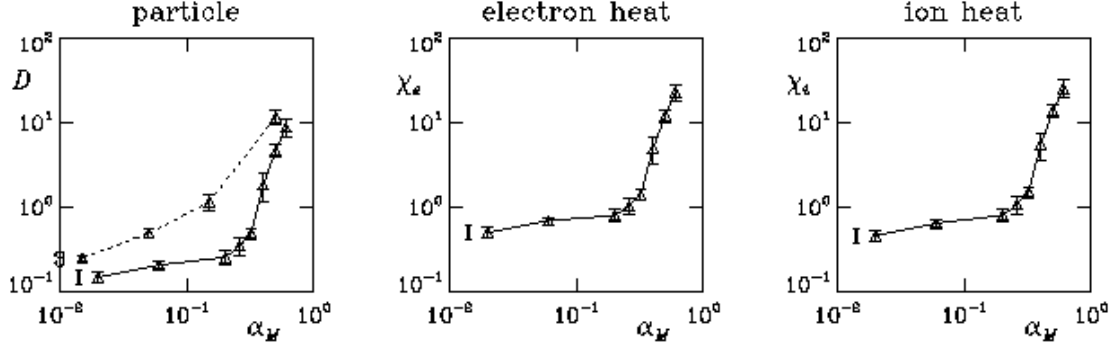


Figure 23. Transport scaling as a function of the ideal ballooning parameter  $\alpha_M$ , for the DALF3 ('3') and DALFTI ('I') models, expressed as diffusivities, with  $\chi_{e,i}$  including the convective contributions. The collisionality was  $C = 2.55$ , in the drift wave regime. The transport is given in physical units ( $\text{m}^2/\text{sec}$ , assuming deuterium ions, and  $B = 2.5 \text{ T}$ , and  $L_\perp = 4.2 \text{ cm}$ ), compensating for the effect of varying  $\hat{\beta}$  on the normalisation scale  $\rho_s^2 c_s / L_\perp$ . The ion temperature assists the transition to ideal MHD in the measure and for the same reason as for the resistive ballooning cases: more total pressure gradient, and  $\tilde{T}_i > \tilde{T}_e$ . But the ideal ballooning threshold, now between 0.2 and 0.6, is lowered by a factor of at least two relative to the linear analysis. The experimentally interesting range is actually  $\alpha_M > 0.2$ , corresponding to  $\hat{\beta} > 1$  for the DALFTI model.

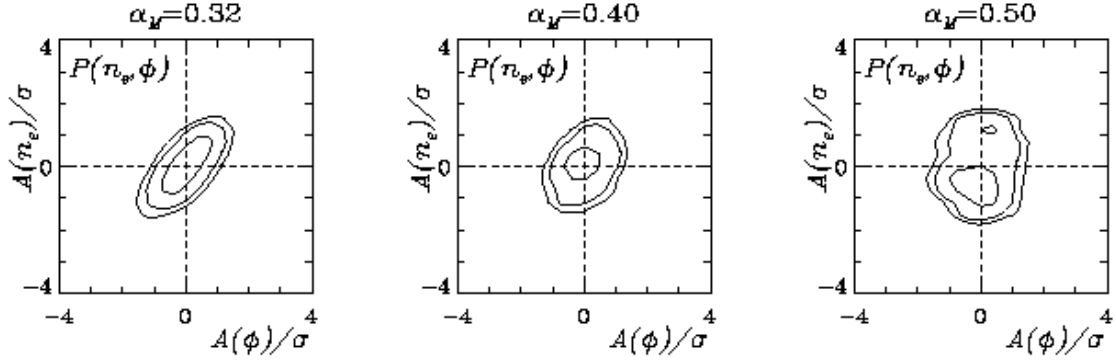


Figure 24. Cross coherence between  $\tilde{n}_e$  and  $\tilde{\phi}$ , for the DALFTI model at  $C = 2.55$  hence  $\nu_B = 0.25$ , for various  $\alpha_M$  in the range of the sharp transport rise, noting  $\alpha_M = 0.2\hat{\beta}$ . The turbulence makes the transition from drift wave to ideal ballooning mode structure in this parameter range. Compare to Fig. 20.



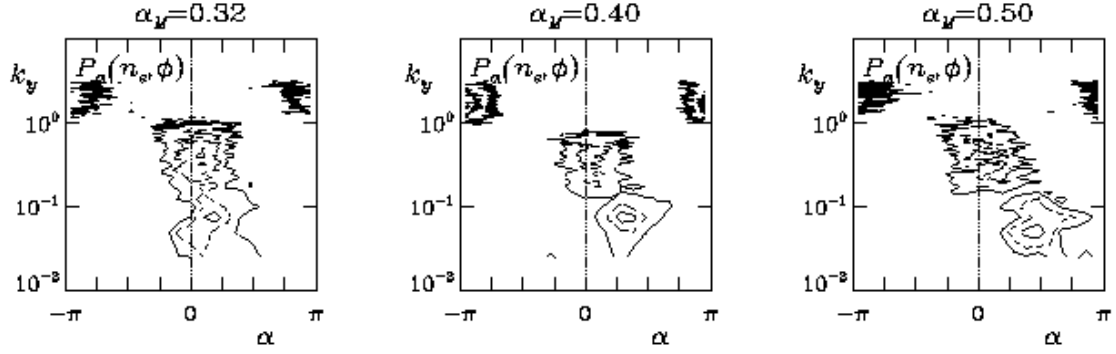


Figure 25. Phase shift distributions of  $\tilde{n}_e$  ahead of  $\tilde{\phi}$  at each  $k_y$ , for the DALFTI model at  $C = 2.55$  hence  $\nu_B = 0.25$ , for various  $\alpha_M$  in the range of the sharp transport rise, noting  $\alpha_M = 0.2\hat{\beta}$ . The turbulence makes the transition from drift wave to ideal ballooning mode structure in this parameter range. Compare to Fig. 21. Here as well, the transition to resistive ballooning turbulence in the DALF3 model occurs in the longest wavelengths,  $k_y\rho_s < 0.1$ .

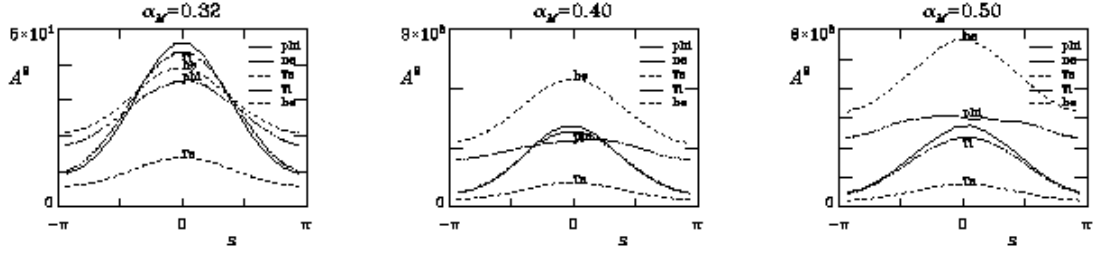


Figure 26. Mean squared amplitude envelopes ( $k_y \neq 0$  only) showing parallel structure of  $\tilde{\phi}$ ,  $\tilde{n}_e$ ,  $\tilde{T}_e$ , and  $\tilde{T}_i$ , respectively labelled by ‘phi’, ‘ne’, ‘Te’, and ‘Ti’, for the DALFTI model at  $C = 2.55$  hence  $\nu_B = 0.25$ , for various  $\alpha_M$  in the range of the sharp transport rise, noting  $\alpha_M = 0.2\hat{\beta}$ . The turbulence makes the transition from drift wave to ideal ballooning mode structure in this parameter range. Compare to Fig. 22. Note  $\tilde{p}_e = \tilde{n}_e + \tilde{T}_e$  and  $\tilde{p}_i = \tau_i \tilde{n}_e + \tilde{T}_i$  in this model.